

1 **Single cell spatial analysis reveals inflammatory foci of immature neutrophil**  
2 **and CD8 T cells in COVID-19 lungs**

3  
4 Praveen Weeratunga<sup>1</sup>, Laura Denney<sup>1</sup>, Joshua A. Bull<sup>2</sup>, Emmanouela Repapi<sup>3</sup>, Martin Sergeant<sup>3</sup>, Rachel  
5 Etherington<sup>1</sup>, Chaitanya Vuppusetty<sup>1</sup>, Gareth D.H. Turner<sup>4</sup>, Colin Clelland<sup>5</sup>, Jeongmin Woo<sup>1</sup>, Amy  
6 Cross<sup>6</sup>, Fadi Issa<sup>6</sup>, Carlos Eduardo de Andrea<sup>7</sup>, Ignacio Melero Bermejo<sup>7</sup>, David Sims<sup>3</sup>, Simon  
7 McGowan<sup>3</sup>, Yasemin-Xiomara Zurke<sup>8</sup>, David J. Ahern<sup>8</sup>, Eddie C Gamez<sup>9</sup>, Justin Whalley<sup>9</sup>, Duncan  
8 Richards<sup>10</sup>, Paul Klenerman<sup>11</sup>, Claudia Monaco<sup>8</sup>, Irina A. Udalova<sup>8</sup>, Tao Dong<sup>1,12</sup>, Agne Antanaviciute<sup>1</sup>,  
9 Graham Ogg<sup>1,12</sup>, Julian C. Knight<sup>9,12</sup>, Helen M. Byrne<sup>2,13</sup>, \*Stephen Taylor<sup>3</sup>, & \*Ling-Pei Ho<sup>1,12,14</sup>.

10  
11 These authors contributed equally: Praveen Weeratunga, Laura Denney, Joshua A. Bull and  
12 Emmanouela Repapi

13  
14 Corresponding authors

15 [Stephen.Taylor@well.ox.ac.uk](mailto:Stephen.Taylor@well.ox.ac.uk)

16 [Ling-pei.ho@imm.ox.ac.uk](mailto:Ling-pei.ho@imm.ox.ac.uk)

17  
18 **Affiliations**

- 19 1. MRC Human Immunology Unit, MRC Weatherall Institute of Molecular Medicine, University  
20 of Oxford, UK  
21 2. Wolfson Centre for Mathematical Biology, Mathematical Institute, University of Oxford, UK  
22 3. MRC WIMM Computational Biology Unit, MRC Weatherall Institute of Molecular Medicine,  
23 University of Oxford, UK  
24 4. Department of Cellular Pathology and Radcliffe Department of Medicine, Oxford University  
25 Hospitals NHS Foundation Trust, UK  
26 5. Anatomic Pathology, Weill Cornell Medical College, Doha, Qatar  
27 6. Nuffield Department of Surgical Sciences, University of Oxford, UK  
28 7. Navarra Institute for Health Research, Pamplona, Spain  
29 8. Kennedy Institute for Rheumatology, University of Oxford, UK  
30 9. Wellcome Centre for Human Genetics, Nuffield Department of Medicine, University of  
31 Oxford, UK  
32 10. Nuffield Department of Orthopedics, Rheumatology and Musculoskeletal Diseases,  
33 University of Oxford, UK  
34 11. Nuffield Department of Medicine, University of Oxford, UK  
35 12. Chinese Academy of Medical Science (CAMS) Oxford Institute (COI), University of Oxford,  
36 Oxford, UK  
37 13. Ludwig Institute for Cancer Research, University of Oxford, UK  
38 14. Respiratory Medicine, Nuffield Department of Medicine, University of Oxford, UK.

44 **Abstract**

45

46

47 Single cell spatial interrogation of the immune-structural interactions in COVID -19 lungs is challenging,  
48 mainly because of the marked cellular infiltrate and architecturally distorted microstructure. To  
49 address this, we develop a suite of mathematical tools to search for statistically significant co-locations  
50 amongst immune and structural cells identified using 37-plex imaging mass cytometry. This unbiased  
51 method reveals a cellular map interleaved with an inflammatory network of immature neutrophils,  
52 cytotoxic CD8 T cells, megakaryocytes and monocytes co-located with regenerating alveolar  
53 progenitors and endothelium. Of note, a highly active cluster of immature neutrophils and CD8 T cells,  
54 is found spatially linked with alveolar progenitor cells, and temporally with the diffuse alveolar damage  
55 stage. These findings offer further insights into how immune cells interact in the lungs of severe  
56 COVID-19 disease. We provide our pipeline [Spatial Omics Oxford Pipeline (SpOOx)] and visual-  
57 analytical tool, Multi-Dimensional Viewer (MDV) software, as a resource for spatial analysis.

58

59

60

61

62

63

64

65

66

67

68

69

70

71

72

73

74

75

76

77

78

79

80

81

82

83

84

85

86

87 **Introduction**

88

89 Since the first reports of COVID-19 cases in Dec 2019, the severe acute respiratory syndrome  
90 coronavirus 2 (SARS-CoV-2) has caused more than 6 million deaths worldwide<sup>1</sup>, mainly from  
91 respiratory failure. Similarities between COVID-19 and other viral infections of the lungs like SARS and  
92 influenza have been noted, but there are specific differences which may be indicative of underlying  
93 disease mechanisms unique to COVID-19. In particular, patients with COVID-19 have excess incidence  
94 of thromboembolic disease, endothelial damage, and greater acute and long-term impact on organs  
95 other than lungs<sup>2-5</sup>. High-resolution immune studies in the blood have shed light on the potential  
96 mechanisms for severe COVID-19 disease, with evidence supporting myeloid cell overactivation and  
97 dysregulation, T cell exhaustion and cytokine hyperactivation<sup>6-10</sup>. Our recent comprehensive multi-  
98 modal study of circulating immune cells (COMBAT study)<sup>6</sup> and several other major studies have also  
99 concluded that a key hallmark of severity was emergency myelopoiesis<sup>6,8,9,11,12</sup>, characterized by raised  
100 circulating immature neutrophils, cycling monocytes, and raised haematopoietic progenitors.  
101 However, it is not known how these findings in blood relate to damaged lung structural cells and other  
102 immune cells in the lungs, nor if they formed injurious immune entities.

103

104 Interrogation of the immune response in COVID -19 lungs have lagged behind studies in peripheral  
105 blood. Our understanding of the immune response in the lungs is derived mostly from several single  
106 cell and single nucleus RNA sequencing studies which have provided valuable insights on a  
107 transcriptomic level<sup>13-18</sup>. However, these are limited by a lack of high resolution (cell level) spatial  
108 context. Transcriptomics studies are also restricted by a lower detection rate for neutrophils as these  
109 cells possess relatively low RNA content and high levels of RNases and other inhibitory compounds  
110 which confound their identification. Notwithstanding these limitations, studies in intact COVID-19  
111 lung tissue are also challenging, due to the distorted lung micro-architecture and massive cellular  
112 infiltrate, making it difficult to unravel cellular connectivity and organisation. An initial evaluation of  
113 COVID-19 lung tissue using imaging mass cytometry by Rendeiro et al concluded that there was  
114 greater spatial proximity between macrophages, stromal cells and fibroblasts in lung samples  
115 obtained later in infection but did not identify reveal further insight into the cause of severe alveolar  
116 damage<sup>19</sup>.

117

118 In this study, we develop a bespoke mathematical package to identify statistically significant co-  
119 location between different cells, including structural cells, at the level of single cell resolution. We  
120 identify a cluster of closely apposed immature neutrophils and CD8 T cells with high immune activity,

121 which are spatio-temporally associated with proliferating alveolar epithelium in tissue sections  
122 demonstrating diffuse alveolar damage. These findings raise the possibility of an injurious entity  
123 generated by the interaction between immature neutrophils and a specific subset of CD8 T cells in  
124 severe COVID-19 pneumonitis.

125

126

## 127 **RESULTS**

128

### 129 **An integrated pipeline to uncover and quantify spatial association amongst cells**

130

131 Our first task was to establish a method to quantify statistically significant spatial correlations between  
132 highly-resolved immune and structural cell types in our lung tissue sections. To do this, we developed  
133 an analytical pipeline which combined an immunology-centric annotation approach with a 3-step  
134 spatial association analysis [quadrat correlation matrices (QCMs), cross-pair correlation functions  
135 (cross- PCFs) and adjacency cell network (ACN)] to provide a set of statistically rigorous spatial  
136 analytical output (Fig. 1A and Supplementary Fig. 1, and described in detail in Methods). In brief, we  
137 first used the QCM to identify cell pairs that are statistically significantly correlated in cell counts.  
138 Correlated cell pairs, of types A and B say, were then examined for co-location above random spatial  
139 association (using cross-PCF). If the cross-PCF,  $g(r)$ , is greater than 1, then cells of type B are observed  
140 more frequently at distance  $r$  from cells of type A than would be expected under complete spatial  
141 randomness (CSR). We considered  $g(r=20)$ , the value of the cross-PCF at  $r=20$ , as a means of  
142 quantifying how many more cells of type B are observed at distance  $20\mu\text{m}$  from an anchor cell of type  
143 A than under CSR. We then examined whether the co-locating cell pairs were physically in contact  
144 with each other using a spatially embedded 'adjacency cell network' (ACN). Using the ACN, we  
145 computed the proportion of cells of type A that were in contact with at least one cell of type B, (full  
146 description found in Methods).

147

148 These work packages were integrated computationally into a workflow of Python and R based  
149 command line tools which may be run individually or as an automated pipeline (Spatial Omics Oxford  
150 pipeline; SpOOx) (Fig. 1A). The pipeline is supported by a visualisation platform [Multi-Dimensional  
151 Viewer (MDV)] (Video V1). Both are available as an open access online resource (see Methods for link).  
152 To differentiate this lung-based from our blood-based study (COMBAT)<sup>6</sup>, we have called this the  
153 COSMIC (CCOVID-19 Lung Single Cell Mass Cytometry Imaging Consortium) study.

154

155

156

157 **Histopathology states of inflammation, damage and repair are found in lung sections at point of**  
158 **death**

159

160 We started by examining formalin-fixed paraffin-embedded (FFPE) lung sections from a cohort of  
161 patients who died from PCR-positive COVID-19 pneumonitis from one hospital (University of Navarra,  
162 Spain) (n=12). Samples were obtained at the point of death and fixed immediately, markedly reducing  
163 post-mortem tissue deterioration<sup>20</sup>. All samples were collected during the first wave of the pandemic  
164 in 2020, before vaccination and repeat infection with SARS-CoV-2. Healthy lung sections from patients  
165 undergoing lobectomy for early, isolated lung cancer (HC) lungs (n=2) were used as comparators  
166 (Demographics in Supplementary Table 1); obtained from the Oxford Radcliffe Biobank (Oxford  
167 University Hospitals NHS Foundation Trust, UK).

168

169 Six of 12 patients were mechanically ventilated (range 6-23 days). All but three were receiving  
170 corticosteroids at the point of death (Supplementary Table 1). In all patients, thoracic CT scans closest  
171 to the day of death demonstrated typical and extensive COVID-19 pneumonitis comprising ground  
172 glass changes and consolidation (Supplementary Table 1). Five of 12 lung sections showed evidence  
173 of both PCR and immunostaining for SARS-CoV2 Nucleocapsid protein; 3 were PCR+ but protein  
174 negative (Supplementary Table 2). Four sequential lung sections (6 µm thick) were used for  
175 haematoxylin and eosin (H&E), 37-plex panel staining (35 metal-tagged antibodies and 2 DNA  
176 chelators), and selected immunofluorescence validation sequentially.

177

178 Initial histopathology analysis (independently performed by two senior pathologists with expertise in  
179 lung and infectious disease, and a senior respiratory clinician) revealed a highly distorted lung  
180 architecture with extensive cellular infiltrate in all samples, changes previously observed in post  
181 mortem studies of COVID-19 lung sections<sup>21-26</sup>. However, all our sections can be categorised into three  
182 formal histopathology classifications of predominantly alveolitis (ALV), diffuse alveolar damage (DAD)  
183 or organising pneumonia (OP) (n=4 patients in each category)<sup>27,28</sup> (Fig. 1B and Supplementary Fig. 2).  
184 ALV was characterised by thickened alveolar epithelial wall and septae with immune cell infiltrate and  
185 congestion of alveolar walls; DAD, by widespread alveolar epithelial lining injury accompanied by  
186 hyaline membrane, regenerating/proliferating Type II alveolar epithelium and interstitial oedema,  
187 while OP depicts a repair state typified by presence of fibroblasts, proliferation of alveolar epithelium  
188 and collagen presence around bronchial epithelium<sup>28</sup>. In keeping with this, patients with dominant

189 OP histopathology showed a trend of being sampled furthest away from their first symptoms (Fig. 1C),  
190 had longer periods of stay in hospital and were mechanically ventilated for longer (Supplementary  
191 Table 1 and Supplementary Fig. 3) (no statistical difference observed). All 5 patients with evidence of  
192 dual SARS-CoV-2 N protein and PCR expression had lung sections that showed DAD. No sections with  
193 OP were positive for SARS-CoV-2 protein staining (Supplementary Table 2; Supplementary Fig. 4).  
194 There were no associations between histopathology states and clinical features (age, drugs used, co-  
195 morbidities, or C-reactive protein (CRP) nearest the point of death) (Supplementary Table 1, Fig. 1D).  
196  
197 These results provide a histopathology-based temporally progressive states for further analysis. 2-3  
198 regions of interest (ROIs) per patient (total of 4 mm<sup>2</sup> area per patient), selected as representative  
199 areas for the dominant histopathology state, were drawn for ablation.

200

#### 201 **Identification of immature neutrophils - CD8 T cell clusters with high immune activity.**

202

203 After preliminary staining with an initial panel (Supplementary Table 3, Supplementary Fig. 5) on a  
204 'sentinel' cohort, we designed a final panel which incorporated the most abundant structural and  
205 immune cell types (Supplementary Fig. 7A). Single cell segmentation performed using Mesmer library  
206 from the DeepCell algorithm<sup>29</sup> resulted in 677,623 single cells from all ROIs, [ALV (n=10 ROIs), DAD  
207 (n=8), OP (n=8) and HC (n=4)] (Fig. 2A, Supplementary Fig. 7 and 12). Cell clusters were derived using  
208 Phenograph and annotation was performed using a combination of expression heat map analyses and  
209 expression density plots (Supplementary Fig. 7). Final annotation was refined with Pseudotime  
210 analysis of selected groups of cell clusters, examination of distributions of the cell clusters in all  
211 samples, and cross-checking with H&E and MiniCAD Design (MCD) images (generated by the Hyperion  
212 imaging system) against known structural cell location and cell morphology (Supplementary Fig. 7).  
213 This produced a final list of 37 identifiable cell clusters (26 immune cell types and 11 structural) (Fig.  
214 2B-C). Expanded description of the annotated cells is provided in Supplementary Table 4. For clarity  
215 of terminology, once the cell clusters were annotated, they were termed 'cell types' or 'cells' unless  
216 there were more than two cell types in the annotation.

217

218 Compared with healthy lungs (without dividing into different histopathology states), monocytes were  
219 the most abundant immune cells (Fig. 2B). Amongst the annotated cell types, five were found to co-  
220 express defining markers of different immune or structural cells, reflecting closely located or apposed  
221 cell groups (Neutrophil and CD8 T cell, Monocyte and CD31<sup>+</sup> cells, Monocyte- PAI-1<sup>+</sup> cells, CD8 T cells  
222 – PAI-1<sup>+</sup> cells and IFN- $\gamma^{\text{hi}}$  cells and RAGE<sup>+</sup> cells). We labelled these 'adjacent' (ADJ) cell types.

223 Immunofluorescence staining confirmed presence of two different adjacent cells for the  
224 Neut\_CD8\_ADJ (immature neutrophil and CD8 T cells) (Fig. 2D, and Supplementary Fig. 7L).  
225 Mono\_CD31\_ADJ comprised both monocytes that were found adjacent to endothelial cells and CD31-  
226 expressing monocytes (Fig. 2E).

227

228 Of note, the Neut\_CD8\_ADJ cells contained the most immature neutrophil cell type (CD71<sup>hi</sup>  
229 neutrophils) coupled with CD45RO<sup>+</sup> CD107a<sup>-</sup>CD8 T cells (Fig. 2F). The cluster also had the highest  
230 expression of Granzyme B (GZB), CD172a (SIRPA), IFN- $\beta$  and IFN- $\gamma$  (Fig. 2F, G-I). Within the cluster, the  
231 GZB expression was found on the CD8 T cells, indicating these as cytotoxic CD8 T cells (Fig. 2I). The  
232 monocyte subset in the Mono\_CD31\_ADJ cluster was the least differentiated (to macrophage)  
233 monocyte subset; similar to the Mono\_1 cell type (Fig. 2D, Supplementary Fig. 7L).

234

### 235 **High innate immune cell numbers found in all histopathology states**

236

237 We next sought to understand how immune cell abundance changed as the overall histology  
238 progresses from injury to repair. Firstly, we observed that changes in numbers of structural and  
239 relevant immune cells supported the temporal progression of histopathology states from inflammation  
240 to damage and subsequent repair (Fig. 3A). There was a progressive increase in numbers of all subsets  
241 of macrophages, fibroblasts, proliferating fibroblasts and myofibroblasts from ALV to DAD to OP,  
242 consistent with transition from tissue injury to repair. Endothelial and proliferating endothelial cells,  
243 proliferating bronchial epithelium and bronchial epithelium also increased progressively. Changes in  
244 abundance of macrophages over the three histopathology states reflected accumulation of  
245 macrophages as monocytes differentiate into macrophages with progression of disease.

246

247 Across the three histopathology states, we found high numbers of classical monocytes, immature  
248 neutrophils, and some subsets of MAIT, CD4 and CD8 T cells. The most significant progressive increase  
249 in numbers across the histopathological states (compared to healthy lungs) was observed for CD8 T  
250 cell subsets and CD8 containing ADJ cell clusters, and CD107a<sup>+</sup> CD4 T cells (Fig. 3B-D) (see  
251 Supplementary Table 4 for expanded phenotype description of immune cell types). Neut\_CD8\_ADJ  
252 cluster was increased from the earliest histopathology state and remained high in all states. Apart from  
253 IFN- $\gamma$ <sup>lo</sup> MAIT cells, there were only small numbers of MAIT and NK cell subsets (Fig. 3C). Cycling (Ki67<sup>+</sup>)  
254 monocytes were not found in the lungs.

255

256 Overall, innate cell numbers in the infiltrate did not decline despite disease progression and was  
257 accompanied by increasing numbers of CD8 T cells [even though viral protein was absent in OP (repair  
258 samples]. Some immune correlates of severity in the blood observed in other studies (cycling  
259 monocytes, NK cells, and activated MAIT cells) were not found in significant numbers in the lungs.

260

### 261 **Distinct spatial organisation found between immune and structural cells**

262

263 To determine if the cells showed spatial association and organisation amongst themselves, we  
264 employed spatial statistical algorithms (Fig. 1A and Supplementary Fig. 1) to (a) understand which  
265 immune cells were found co-located with injured structural cells, (b) explore how immune cells  
266 organise themselves amongst themselves, and (c) for the immune cells implicated in severe disease  
267 from COMBAT (monocyte, megakaryocyte, MAIT, CD4, CD8 and neutrophil subsets), if these were co-  
268 located or physically interacting with other immune or structural cells

269

270 In total, we found 3888 non-replicate pairs of cell types (mono1:mono1 and CD15<sup>hi</sup> iNeut:CD15<sup>hi</sup> iNeut  
271 were examples of pairs of identical cell types, and filtered out) in the three histopathological states  
272 (ALV, DAD and OP). Using our three-step spatial analysis, 357 pairs of cell types were identified as  
273 statistically correlated in the QCM analysis (FDR <0.05). These cell pairs were submitted for cross- PCF  
274 analysis, with one cell type in the pair defined as the 'anchor cell' -the cell against which statistically  
275 significant connections were quantified. By pre-analysis consensus, pairs of cell types with borderline  
276 statistical significance i.e. FDR values between 0.05 and 0.10 were also submitted to prevent loss of  
277 biologically relevant data from hard mathematical cut-off. The resulting co-located cell pairs were  
278 divided into 'structure:immune' pairs (structural cells were designated the 'anchor' cell type) (n=33)  
279 and 'immune: immune' pairs (one cell type in one of the duplicate pairs was designated the anchor  
280 cell type; e.g. for the CD107a<sup>+</sup>CD8:mono1 pair and mono1: CD107a<sup>+</sup>CD8 pair; CD107<sup>+</sup>CD8 in the former  
281 pair was made the anchor cell, and the latter pair was excluded) (n=117) (Fig. 4A). 'Structure' cells of  
282 interest were the key structural cells that were known to be inflamed or damaged in COVID-19  
283 pneumonitis – endothelium ('Endothelium' and 'proliferating endothelium') and larger blood vessels  
284 ('blood vessels'), alveolar epithelial cells ('proliferating alveolar epithelium') and bronchial epithelial  
285 cells ('HLA DR<sup>hi</sup> bronchial epithelium' 'HLA DR<sup>lo</sup> bronchial epithelium' and 'bronchial epithelium'). We  
286 were particularly interested in 'proliferating alveolar epithelium' as their markers and location in the  
287 lung sections suggest they were likely the type II alveolar epithelial cells, the purported progenitors  
288 (or stem cells) of alveolar epithelium (Supplementary Fig. 7J and K). The ability of these cells to



289 differentiate to type 1 alveolar epithelium is critical to normal repair and alveolar regeneration after  
290 viral induced damage<sup>30-32</sup>.

291

292 Amongst the immune cells, the strongest co-location, depicted by  $g(r=20) > 2$  [i.e.  $> 2$  times more cells  
293 of type B observed at 20  $\mu\text{m}$  from cells of type A (anchor cell) than expected under complete spatial  
294 randomness], was observed for pairs of immune cell types that belonged to the same immune  
295 phenotype, e.g. Mac1 and Mac2 (macrophages), and the CD4 and CD8 T cell types (Fig. 4B). This was  
296 expected biologically and provided a degree of validation for the mathematical analysis. For example,  
297 close association between helper CD4 T cells (IFN- $\gamma^+$  CD4 T cells) and cytotoxic CD8 T cells (CD107a+  
298 CD8 T cells) is expected as the former plays critical roles in aiding the latter's anti-viral activities.  
299 However it is notable that this close physical relationship persists in OP, despite lack of viral protein at  
300 this stage of the disease (Supplementary Fig. 9).

301

302 These results signify presence of specific spatial organisation for several immune and structural cells  
303 despite appearance of disorder in tissue. The strongest co-location between all cells was found  
304 between CD4 and CD8 T cell subsets, particularly active effector memory CD4 T cells (IFN- $\gamma^+$  CD4 T  
305 cells) and cytotoxic CD8 T cells (CD107a<sup>+</sup> CD8 T cells), which did not lessen with progression to repair,  
306 and despite absence of viral proteins.

307

308 **Immature neutrophil-CD8 T clusters are co-located with proliferating alveolar epithelium in regions**  
309 **with maximal alveolar damage**

310

311 For the significantly co-located pairs of cells, we next questioned which immune cells were found co-  
312 located with injured structural cells. To provide a composite view of the multiple output from our  
313 spatial analysis, we generated a 'spatial connectivity plot' to show all cell types that were statistically  
314 co-located with a designated 'anchor cell type'. Each spatial connectivity plot displayed the strength  
315 of co-location [ $g(r=20)$ ] and the average count for the immune cell types in the histopathology state  
316 (Fig. 5A, B). The proportions of co-locating cell types which were in direct contact with the anchor cell  
317 type were calculated with the ACN analysis (see Methods) and shown in the accompanying histograms  
318 (Fig. 5C and D).

319

320 Our main structural cell types of interest were the Ki67<sup>+</sup> proliferating alveolar epithelial cell and  
321 endothelial cells. Designating proliferating alveolar epithelium as the anchor cell, we found CD15<sup>hi</sup>  
322 iNeut, Mono\_CD31\_ADJ and Neut\_CD8\_ADJ to be significantly co-located with proliferating alveolar

323 epithelium in DAD (Fig. 5A, B) [ $g(r=20)>1$ ]. Of these cells, proliferating alveolar epithelium was most in  
324 contact with Mono\_CD31\_ADJ (average of 17.6% of proliferating alveolar epithelial cells in DAD) and  
325 Neut\_CD8\_ADJ (8.9% of proliferating alveolar epithelial cells in DAD) (Fig. 5C). There was also a small  
326 number of IFN- $\gamma^{\text{hi}}$ \_RAGE\_ADJ cells found co-located with proliferating alveolar epithelium in all  
327 histopathology states, which could be resident alveolar macrophages found along alveolar epithelium.

328

329 For endothelial cells (which encompassed the smaller capillaries and the larger blood vessels in the  
330 lungs), the co-locating cell types with highest  $g(r=20)$  in DAD were Mono\_CD31\_ADJ (2.1) and  
331 Mono\_PAI-1\_ADJ (1.6) clusters (Fig. 5B,F). ACN analysis showed more of the endothelial cells were  
332 physically in contact with the Mono\_PAI-1\_ADJ cluster (21.2%) than Mono\_CD31\_ADJ (16.5%) in DAD  
333 (Fig. 5D). Mono\_CD31\_ADJ cells showed significant spatial association with endothelial cells across all  
334 histopathology states.

335

336 Next, we designed a 'radial connectivity map' to provide an overview of all immune cells that were  
337 significantly co-located with all structural cells and their corresponding histopathology states (Fig. 5G).  
338 Using this map, and focusing on proliferating alveolar epithelium and endothelial cells, we observed  
339 that while the monocytes (and their subsets and ADJ clusters) were mainly found co-located with both  
340 alveolar epithelium and endothelial cells, immature neutrophils were found predominantly with  
341 proliferating alveolar epithelium. We also observed that besides proliferating alveolar epithelium, the  
342 Neut\_CD8\_ADJ cluster was not found with any other structural cell types.

343

344 Finally, we developed a topographical correlation map (TCM) (Methods, Supplementary Fig. 15) to  
345 visualise how the spatial correlation between Neut\_CD8\_ADJ and proliferating alveolar epithelium  
346 changed across an ROI (Fig. 5H). We observed marked heterogeneity in the strength of correlation for  
347 this pair of cell types across the tissue.

348

349 One other cell type of interest was the megakaryocyte. These CD34<sup>-</sup> platelet precursors, a product of  
350 emergency myelopoiesis, were the most abundant immune correlate in the blood in the COMBAT  
351 study <sup>6</sup>. Examining their spatial connections with our two structural cells of interest, we observed  
352 that megakaryocytes were associated with endothelium in DAD (Fig. 5G).

353

354 Drawing these data together, our spatial analysis identified Neut\_CD8\_ADJ and Mono\_CD31\_ADJ  
355 clusters as key spatial correlates with proliferating alveolar epithelium in DAD. A visual exemplar of  
356 this co-location of Neut\_CD8\_ADJ and alveolar epithelium is shown in Fig. 5I. Mono\_CD31\_ADJ and

357 Mono\_PA1-1\_ADJ were the strongest spatial correlates with endothelial cells, the former was the case  
358 across all states. No immature neutrophils (alone or in an ADJ cluster with CD8 T cells) were found  
359 with endothelial cells in any histopathology states. It is noteworthy that there was no significant co-  
360 location between any immune cells and the larger blood vessels; nor between CD107a<sup>+</sup> CD8 T cells  
361 and IFN- $\gamma$ <sup>+</sup> CD4 T cells with proliferating alveolar epithelium or endothelial cells despite relatively high  
362 abundance in the tissue. In addition, despite a correlation with disease severity in the blood, NK and  
363 MAIT cells did not co-locate with any structural cells. Further, even though macrophage subsets were  
364 the most abundant cells in lungs, there was also no statistically significant co-location between these  
365 cells and damaged structural cells.

366

367 All data, the spatial connectivity plot, radial connectivity map, and topographical correlation map  
368 functions are available as open resources on MDV (<https://mdv.molbiol.ox.ac.uk/>, Supplementary Fig.  
369 10, Methods).

370

### 371 **Immature neutrophils have a spatial predilection for CD8 T cells**

372

373 We next examined how immune cells connected to other immune cells by interrogating the 91 pairs  
374 of immune cells with  $g(r=20)>1$  across the three histopathology states (Fig. 6A-C).

375

376 We observed that as single entities (as opposed to those found within ADJ clusters), immature  
377 neutrophils only co-located with CD8 T cells or CD8-ADJ clusters (Fig. 6A), regardless of histopathology  
378 state. However, immature neutrophils within the Neut\_CD8\_ADJ cluster, co-localised with  
379 Mono\_CD31\_ADJ clusters in DAD and other monocyte subsets in OP (Fig. 6A and D).

380

381 Therefore, in DAD, proliferating alveolar epithelium not only co-located with Neut\_CD8\_ADJ, but also  
382 with a further network of co-locating immune cell types linked to the Neut-CD8\_ADJ cluster, forming  
383 a super network of Neut\_CD8\_ADJ and Mono\_CD31\_ADJ clusters around the proliferating alveolar  
384 epithelial cells. This can be seen in the ACN analysis (Fig. 6F) and an MCD image view of the cells in the  
385 tissue (Fig. 6G).

386

387 In contrast to neutrophils, there was a less restricted repertoire of co-locating cell partners for  
388 monocytes. Monocyte subsets and ADJ clusters were found co-located with NK, MAIT, CD4 and CD8 T  
389 cell subsets (Fig. 6B-C). Notably, megakaryocytes were found uniquely associated with  
390 Mono\_CD31\_ADJ in DAD (Fig. 6E).

391

392 Our analyses showed that there were distinct organisations amongst immune cells in COVID-19 lungs,  
393 with specific predilection of immature neutrophil for CD8 T cells, and upon connection (as the  
394 neutrophil\_CD8\_ADJ cluster), a further connection with Mono\_CD31\_ADJ cluster was formed,  
395 resulting in a network of Neut\_CD8\_ADJ and Mono\_CD31\_ADJ, linked to proliferating alveolar  
396 epithelium in diffuse alveolar damage. These were then linked to megakaryocytes via the latter cell  
397 type's connection with Mono\_CD31\_ADJ cluster in DAD. Thus, a spatial network of immature  
398 neutrophils, CD8 T cells, classical monocytes and megakaryocyte form a connected web of cells  
399 juxtaposed against proliferating alveolar epithelial cells and alveolar capillaries in DAD.

400

401

#### 402 **Projection of the circulating source of lung CD8 T cells, monocytes and immature neutrophils**

403

404 Finally, we returned to our COMBAT data<sup>6</sup> to explore if we can identify the circulating source of the  
405 monocytes, CD8 T cells and neutrophils found in the lungs. Using *scmap*, a method which enables label  
406 projection by calculating the similarity between cells profiled by two separate studies<sup>33</sup>, we examined  
407 the phenotypic similarity between monocytes and CD8 T cells in the lungs [this study (COSMIC)] and  
408 blood (COMBAT study). For COMBAT, we used the CYTOF dataset from neutrophil-depleted whole  
409 blood ( Supplementary Fig. 3 in COMBAT)<sup>6</sup>.

410

411 Both lung CD107a<sup>-</sup> CD8 and CD107a<sup>+</sup> CD8 matched to blood 'GZB<sup>neg</sup> CD8 T cells' in COMBAT (Fig. 7A).  
412 Lung IFN- $\gamma$ <sup>+</sup> CD4 T cells matched to COMBAT's 'activated CD4 T cells' subset (which contained CD27<sup>-</sup>  
413 and CD27<sup>+</sup> CD4 T cells). All monocyte subsets in the lung [including Mono\_CD31\_ADJ, Mono\_PA1-  
414 1\_ADJ (but not Mono3)], and all macrophage subsets showed high Jaccard similarity index with HLA  
415 DR<sup>hi</sup> classical monocytes in the blood (Fig. 7B).

416

417 We next interrogated the markers for these two COMBAT cell types (GZB<sup>neg</sup> CD8 T cells and HLA  
418 DR<sup>hi</sup> classical monocytes) (data found in Supplementary Data 3 in COMBAT). We observed that  
419 compared to healthy and disease controls, GZB<sup>neg</sup> CD8 T cells expressed markers of exhaustion and  
420 were KLRG1<sup>+</sup> compared to other CD8 T cells. HLA DR<sup>hi</sup> classical monocytes showed high expression of  
421 CLA. Both GZB<sup>neg</sup> CD8 T cells and HLA DR<sup>hi</sup> classical monocytes were unique amongst CD8 T cell and  
422 monocyte subsets in showing lower abundance in COVID-19 patients compared to healthy  
423 volunteers<sup>6</sup>, raising the possibility that these were the subsets that have trafficked to the lungs. This

424 is not unprecedented given previous findings in lungs which showed sparse antigen-specific T cells in  
425 blood of severe influenza patients but 8 times higher in matched blood-lung samples<sup>34</sup>.

426

427 For neutrophil comparisons between lungs (COSMIC) and blood (COMBAT), we obtained stored whole  
428 blood samples and stained these with a 42-marker CYTOF panel (Supplementary Table 5). 8  
429 subclusters of neutrophils were evident from dimensionality reduction (UMAP) and unsupervised  
430 clustering, and annotated according to maturity – from pro-neutrophil to mature neutrophils (Fig. 7C-  
431 D). Compared to the lung neutrophils, ‘immature neutrophil 2’ in the blood (which expressed the  
432 highest level of CD172a amongst the immature CD10<sup>+</sup> neutrophil subsets), most closely matched the  
433 neutrophil subset in Neut\_CD8\_ADJ (Fig. 2F). Notably, the abundance of ‘immature neutrophil 2’  
434 correlated positively with severity of disease (Fig. 7E).

435

436 These findings showed that the lung CD8 T cell subsets matched most closely to a GZB<sup>neg</sup> KLRG1<sup>+</sup> CD8  
437 T cell subset in the blood, which also expressed a T cell exhaustion signature. This suggests that this  
438 blood CD8 T cell subset is a likely source for the GZB<sup>+</sup> CD8 T cells found in the Neut\_CD8\_ADJ cluster;  
439 and that within this cluster, CD8 T cells expressed GZB, possibly with exposure to IFN- $\beta$ <sup>35</sup>. On the other  
440 hand, blood CD172a<sup>hi</sup> immature neutrophil subset is the likely source for the immature neutrophils in  
441 the lungs, including that found in the Neut\_CD8\_ADJ cluster.

442

443

#### 444 **Discussion**

445

446 In this paper, we deconvoluted a highly disordered immune and structural landscape to provide  
447 accurate annotations and abundance metrics for the cellular landscape and then leveraged  
448 mathematical techniques to describe co – location and cell contact-based network construction. Our  
449 mathematical tools encompassed a range of spatial statistics and methods from network science;  
450 some transposed from ecology<sup>36-38</sup>. The pipeline uncovered a hitherto undescribed physical  
451 partnership between immature neutrophils and CD8 T cells in COVID-19 lungs linked to proliferating  
452 alveolar epithelium in areas with diffuse alveolar damage. This further connected with classical  
453 monocytes and megakaryocyte around endothelial cells, forming a super pro-inflammatory network  
454 across the alveolar bed in DAD. The observations on neutrophils are especially significant since  
455 relatively little is understood of the role of neutrophils in the lungs of patients with COVID-19 due to  
456 poor detection with transcriptomic methods<sup>17,39</sup>.

457

458 Our study did not elucidate how neutrophil-CD8 clustering might contribute to disease pathogenesis.  
459 However, evidence from other diseases provide some insight. Neutrophils and CD8 T cells aggregation  
460 in colorectal cancer and graft vs host disease have been shown to enhance T-cell receptor–triggered  
461 activation of CD8<sup>+</sup> T cells <sup>40</sup> causing neutrophil-mediated tissue damage by the release of reactive  
462 oxygen species <sup>41</sup>. Neutrophils can also act as antigen presenting cell which cross present antigen to  
463 CD8 T cells, further enhancing activation <sup>42,43</sup>. CD8 T cells with a similar effector memory and GZB<sup>+</sup>  
464 profile as that found in the Neut\_CD8\_ADJ cluster have also been implicated in immunopathology of  
465 COVID-19 in other organs. Imaging mass cytometry studies in COVID-19 brain tissue showed intriguing  
466 spatial associations with microglia, which also sustained immune activation and neuroinflammation  
467 <sup>44</sup>.

468  
469 The presence of viral antigen could be the trigger for these foci of immature neutrophils and CD8 T  
470 cells, possibly initiated by recognition of viral antigen by CD8 T cells. However, we note abundant  
471 Neut\_CD8\_ADJ cluster in the OP state (Fig. 3B) where there were no viral proteins or RNA. One  
472 explanation is that these CD8 T cells were self-proliferating, as suggested by Liao’s study using single  
473 cell RNA sequencing of lung-lavaged cells in COVID-19 patients <sup>45</sup>. Supporting this, Neut\_CD8\_ADJ  
474 cluster showed the highest Ki67 expression (Fig. 2F), with MCD imaging isolating this expression to  
475 CD8 T cells (Fig. 2I). Organising pneumonia is not a natural sequela of all viral infection or alveolar  
476 inflammation. Indeed, many patients who do well do not progress to consolidation on computed  
477 tomographic (CT) scans. Thus, a potential deleterious effect of these foci of inflammation could be the  
478 obliteration of regenerative potential in type II alveolar epithelial cells, the purported stem cells for  
479 the alveolar unit <sup>46</sup>, and development of organising pneumonia (OP).

480  
481 Another cluster highlighted by our analyses was the Mono\_CD31\_ADJ cluster, which was spatially  
482 associated with Neut\_CD8\_ADJ cluster, and with proliferating alveolar epithelial cells. Proliferating  
483 alveolar epithelial cells are the nominal stem cells for the alveoli and key to replenishment of type 1  
484 alveolar epithelial cells. Its health, and ability to function optimally, is a key requirement for repair of  
485 infected and damaged alveoli. A consequence could be that the production of type I IFN, [and other  
486 monocyte-specific cytokines like IL-6 and TNF-  $\alpha$  (as reviewed by, <sup>47,48</sup>], combined to impact on  
487 regeneration of alveolar epithelium. It is also possible that type I IFN production from these monocytes  
488 causes upregulation of ACE2, thereby sustaining viral entry and alveolar epithelial damage<sup>49</sup>. This  
489 agrees with observation from transcriptomic studies of the lungs where type II alveolar epithelium  
490 were found in an inflammation-associated intermediate state rather than progressing via normal  
491 regeneration to type I alveolar epithelium <sup>13,15,17</sup>.

492

493

494 The tight association between a large number of monocytes and endothelial cells in all histopathology  
495 states could result in excess inflammation and also predispose to small vessel thrombosis, particularly  
496 with further presence of megakaryocytes at the point of maximal injury (DAD) (Fig. 5B). Single cell  
497 transcriptomic analyses in COVID lungs have demonstrated upregulation of endothelial-damage  
498 markers, including VWF, ICAM1 and VCAM1, and transcriptional programs suggesting altered vessel  
499 wall integrity and widespread activation of coagulation pathway associated genes in endothelial  
500 cells.<sup>13,16,50</sup> In addition, autopsy studies have shown high numbers of megakaryocytes and platelet  
501 rich thrombi in the lungs with COVID-19 pneumonitis<sup>51</sup>.

502

503 Beyond these key messages, other findings clarified the importance of immune cell numbers and  
504 phenotype in blood of patients with severe COVID-19. There was no significant spatial co-location  
505 between activated NK cells and MAIT cells with any structural cells although the numbers for MAIT  
506 cells were increased, in keeping with blood levels. With the ability to identify single cells of CD4 and  
507 CD8 T cells, and quantify their abundance per mm<sup>2</sup> of lungs, we also showed definitively that levels  
508 of CD4 and CD8 T cells were high in lung samples in contrast to studies which inferred their depletion  
509 from gene expression profiles<sup>15</sup>. Immature cycling monocytes, one of the most striking observations  
510 in the blood of patients with severe compared to mild COVID-19 disease<sup>6,8</sup>, were not found in lung  
511 tissue. This suggests that immature monocytes are unlikely to be involved in tissue damage, and  
512 unlike immature neutrophils, probably differentiated rapidly to mature monocytes and  
513 macrophages.

514

515 Our findings refined our earlier work on a smaller subset of COVID-19 lungs (n=3) using targeted  
516 transcriptomic analysis (GeoMx) in specified sections in the lungs linked to alveolar damage<sup>52</sup>. In that  
517 work, we deconvoluted cells detected by gene expression profile using limited protein markers and  
518 showed that CD8 T cells and macrophages with IFN- $\gamma$  signature correlated with areas of lungs with  
519 alveolar damage. Interestingly, areas of severe damage exhibited consistent expression of IFN $\gamma$ -  
520 regulated chemokines such as *CXCL9/10/11* that may promote CXCR3-mediated chemotaxis or  
521 retention of CD8 T effector lymphocytes. Further to the findings from this paper, we performed  
522 additional analyses to determine if we can provide a transcriptomic view of the immature neutrophils  
523 and CD8 T cell cluster. This strengthened but did not reveal further findings (described in  
524 Supplementary Fig. 11).

525

526 Another earlier work in the same lung samples showed significant presence of neutrophil extracellular  
527 traps (NETS) in the lung samples which correlated with areas of low CD8 T cell levels. Re-examining  
528 the number of NETS per lung section, we observed widespread presence with no significant difference  
529 between the three histopathology states (Supplementary Fig. 3C). As NETS production is a feature of  
530 mature rather than immature neutrophils<sup>20</sup>, one explanation is that there is a CD8-directed immature  
531 neutrophil localisation to proliferating alveolar epithelium, which is separate from the relatively less  
532 discriminate NETS expression by mature neutrophils.

533

534 The key limitation of our study is that it is an observation of association, albeit that there was clear  
535 comparison between histopathology characterisations of alveolitis, damage and repair. Thus, it is not  
536 possible to elucidate cause or effect. Further functional studies will strengthen the findings. Our  
537 cohort was also small though this was counterbalanced by uniquely fresh samples from lungs, with  
538 minimal effect of degradation due to the sampling methods at the point of death. Finally, our study  
539 was led by specific questions. To that end, the antibody panels, and analyses were targeted to those  
540 questions and cellular identities were constrained to that linked to the antibody panel.

541

542 We conclude that statistically rigorous analyses of spatial associations of immune and structural cells  
543 in lungs of those with fatal COVID-19 identified an inflammatory nidus of immature neutrophils and  
544 CD8 T cells with high immune activity and proliferating capabilities that were linked to alveolar  
545 progenitor cells in areas with greatest alveolar damage. It establishes the importance of emergency  
546 myelopoiesis in lung immune pathology, with potential roles for immature neutrophils and  
547 megakaryocytes in alveolar damage, aberrant alveolar regeneration, and excess thrombogenesis. The  
548 findings support the evaluation of therapeutics that target monocytes and immature neutrophils,  
549 potentially earlier in disease to limit its impact on progression to widespread alveolar damage and  
550 organising pneumonia. It also means that drugs that increase the longevity or survival of CD8 T cells  
551 require further assessment given the potential contribution of CD8 T cells to lung damage.

552

553

554

555

556

## 557 **Methods**

### 558 **Table of antibodies and reagents used in imaging mass cytometry and immunofluorescence**



559 All antibodies, their catalogue numbers, final dilutions, and source are documented in Supplementary  
560 Data 1.

561

### 562 **Patients, samples, and ethical approvals**

563

564 Lung samples were obtained from collaborators from the University of Navarra, Spain and comprised  
565 those patients who died in hospital after admission with COVID-19. The only inclusion criteria were  
566 (i) hospitalisation, (ii) evidence for COVID-19 pneumonitis, defined as presence of ground glass  
567 changes +/- consolidation and peri bronchial shadowing in mid to peripheral distribution on thoracic  
568 CT scan before death, (iii) PCR+ results for nucleocapsid (N) and/or envelope protein I in lung or liver  
569 tissue sample and (iv) negative bacterial culture from blood and lung within 3 days of death. The study  
570 was approved by the Ethics Committee of the University of Navarra, Spain (Approval 2020.192). Tissue  
571 collections were obtained with consent from a first-degree relative, following a protocol approved by  
572 the ethics committee of the University of Navarra (Protocol 2020.192p); and stored under Spain's  
573 Human Tissue Authority regulations. Samples were collected during the first wave of pandemic (2020)  
574 via an intercostal space incision, using core biopsy methods (BioPince Full Core Biopsy Instrument kit)  
575 immediately after death<sup>20,53</sup>. Tissues were immediately fixed in neutral buffered formalin for over 24  
576 hours, and then paraffin-embedded. These samples were also shared with other collaborators and  
577 studies carried out independently<sup>20,52</sup>.

578

579 Healthy lung controls were obtained from the Oxford Centre for Histopathology Research and the  
580 Oxford Radcliffe Biobank based at the Oxford University NHS Hospitals Foundation Trust. Ethics  
581 approval was received from Oxford A South-Central NHS REC (ref 19/SC/0173). The inclusion criteria  
582 were that lung sections had to be obtained away from localised lung cancer site on lung imaging; they  
583 had to have normal lung histopathology as agreed by two independent histopathologists, aged  
584 between 50-90y and had no concomitant lung diseases. Altogether 8 such patients were identified,  
585 their lung sections stained with H & E and two representative patients selected to proceed to IMC  
586 staining. H & E stained sections are shown in Supplementary Fig. 4.

587

588 We have considered sex balance in selection of samples. There are 5 females and 7 males in our  
589 cohort. Patients and relatives were not financially compensated.

590

### 591 **RNA extraction and quantitative RT-PCR for viral genes**

592

593 RNA extraction from biopsies was performed using the QIAamp Viral RNA Mini Kit (Qiagen) and the  
594 identification of SARS-CoV-2 transcripts encoding nucleocapsid (N) and an envelope protein I was  
595 performed using a commercial kit (SARS-CoV-2 Real Time PCR Kit, Vircell), both according to  
596 manufacturer recommendations, at the Microbiology Laboratory of the Clinica Universidad de  
597 Navarra (ref). Samples with amplification of both targets with Ct values below 35 were considered  
598 positive for SARS-COV-2. Ct threshold was selected based on comparison between Ct values and  
599 presence of viral DNA on nasopharyngeal-swab standards.

600

#### 601 **SARS-CoV-2 Nucleocapsid protein staining**

602

603 Slides were deparaffinised and heat-induced epitope retrieval were performed on the Leica BOND-  
604 RXm using BOND Epitope Retrieval Solution 2 (ER2, pH 9.0) for 30 minutes at 95°C. Staining was  
605 conducted with the Bond Polymer Refine Detection kit, a rabbit anti-SARS-CoV-2 nucleocapsid  
606 antibody (Sinobiological; clone: #001; dilution: 1:5000) and counterstained with haematoxylin.

607

#### 608 **Region of interest (ROI) selection**

609

610 H&E stained sections were examined by two senior pathologists independently and a pulmonologist  
611 and data compiled with consensus at the third iteration. ROIs were selected based on size (2x 2mm  
612 squares or equivalent surface areas) to represent the dominant histopathology findings for the  
613 section. Slides were imaged on AxioScan Z1 slide scanner [Zeiss] and viewed using QuPath<sup>54</sup>

614

#### 615 **Imaging mass cytometry (IMC) staining**

616

617 Sequential 6µm thick FFPE lung tissue section slides were incubated for 2 hours at 60°C on a slide  
618 warmer, dewaxed twice in Histo-clear II (National Diagnostics) for 10 minutes before rehydration  
619 through serial alcohols; 100%, 100%, 95%, 70% ethanol and MilliQ water. Slides were then incubated  
620 for 30 minutes at 96°C in EDTA Target Retrieval Solution, pH 9 (Agilent) and cooled to 70°C before  
621 washing twice in MilliQ water. Slides were blocked in 3% BSA solution in Maxpar PBS (Standard  
622 BioTools; previously Fluidigm) for 45min. Sections were then stained with metal-conjugated  
623 antibodies in Maxpar PBS containing 0.5% BSA overnight. Antibodies conjugated in house were  
624 conjugated with MaxPar X8 antibody labelling kits (Standard BioTools) or Lightning-Link kits (Abcam)  
625 according to manufacturer's instructions. Slides were washed in 0.2% Triton X-100 then twice in

626 Maxpar PBS. Intercalator-Ir (Standard BioTools) diluted in Maxpar PBS was used to stain DNA (30min),  
627 slides were washed in MilliQ water then air dried.

628

629 Ablation of the relevant regions of interest (ROIs) was carried out on Standard BioTools Hyperion  
630 Imaging System using CyTOF7 Software v7.0 (Standard BioTools) and visualized using MCD Viewer  
631 (Standard BioTools). Images were processed for publication using FIJI <sup>55</sup> to de-speckle and sharpen  
632 the images.

633

#### 634 **Antibody validation and optimization**

635

636 Antibody clones were selected which had previously been published and validated in IMC studies as  
637 well as antibodies frequently utilized for immunofluorescence or immunohistochemistry studies with  
638 FFPE tissues. Staining validation for IMC markers was performed in healthy control lung and tonsil as  
639 well as in some COVID-19 infected lung (Supplementary Fig. 5,6 and 12). During optimisation, we  
640 checked that (i) mutually exclusive expression pattern were found in key immune and structural  
641 lineage markers i.e. CD68, Epcam, CD3 and CD19 (ii) markers showed appropriate subcellular location  
642 expression i.e. transcription factors Foxp3 and Ki67 were nuclear, whereas CD68 expression was  
643 cytoplasmic and cell membrane. (iii) structural cell identities defined by IMC lineage marker expression  
644 are compatible with cell morphology and location in H&E. Adjacent H&E-stained slides and structural  
645 markers expression was examined e.g.  $\alpha$ -SMA expression around vessels and bronchi, EpCAM  
646 expression on bronchial and alveolar epithelial cells. (iv) Non-biological sense expression e.g. CD4 and  
647 CD8 co-expression and biologically expected and coherent co-expression patterns eg. cells expressing  
648 CD45, CD3, CD8 and CD45RO were examined (v.) Expression for the following key markers was  
649 validated by immunofluorescence staining in adjacent slides – CD4, CD8, CD14, CD15, CD31, CD172a,  
650 CD206, ProSPC, PAI-1, Epcam and Ki67.

651

652 Antibody clones that did not perform well i.e. those with weak signal, high background, or nonspecific  
653 staining were discarded. Antibody titration was performed to maximise signal to noise ratio in both  
654 lung and tonsil tissues and panels were designed to minimise the already low levels of signal spill over  
655 see in IMC [less than 1-5%] <sup>56</sup>.

656

657

658

659

660 **Immunofluorescence**

661

662 Paraffin-embedded human lung tissue sections were deparaffinized and each section was pre-treated  
663 using heat-mediated antigen epitope retrieval with sodium citrate buffer (pH 6) for 20 minutes. Then  
664 sections were blocked in 10% normal goat serum (Thermo Fischer Scientific, 50062Z) for 20 minutes  
665 and then incubated with CD14 antibody 1:100 dilution (Abcam, AB183322), CD15 antibody 1:200  
666 dilution (Cell signalling Technology, 4744S), CD31 Antibody 1:100 dilution (LS Bio, LS-B15507-LSP), CD8  
667 Antibody 1:100 dilution (Cell signalling Technology, 90257SF), CD172a, Anti- SIRP-Alpha Antibody  
668 1:100 dilution (Abcam AB19149), Pro-Surfactant Protein C Antibody 1:100 dilution (Abcam AB90716),  
669 overnight at 4°C. Each section is washed three times in TBS-T (0.1% Tween) and stained with Alexa  
670 Fluor 568 or 647 conjugated Goat anti Rabbit IgG or Alexa Fluor 488 or 568 conjugated goat anti-  
671 mouse IgM secondary antibody or Alexa Fluor 488, 568 or 647 conjugated goat anti-mouse IgG1 for  
672 30 minutes and washed three times in TBS-T (0.1% Tween) and mounted with Prolong platinum  
673 antifade Mountant with DAPI (Fischer Scientific) and the section slides were imaged using a Nikon Ti2  
674 microscope (Nikon Instruments, Japan) attached to an Andor Dragonfly 200 spinning disk confocal  
675 microscope (Oxford Instruments, Belfast).

676

677 **Imaging of Fluorescent labeled Tissue Sections**

678

679 Slides were imaged using a Nikon Ti2-E microscope (Nikon Instruments, Japan) attached to an Andor  
680 Dragonfly 200 spinning disk confocal unit (Oxford Instruments, Belfast). Using Andor Fusion software,  
681 the microscope was configured for DAPI (Excitation 405 nm: Emission 450/50 nm), GFP (Excitation 488  
682 nm: Emission 525/50 nm), Red (Excitation 561 nm: Emission 600/50 nm) and Far Red (Excitation 647  
683 nm: Emission 700/75 nm). A 10x 0.45 NA objective was initially selected to provide an overview of the  
684 entire area of the tissue section. Relevant areas (or the whole section) were then selected using the  
685 software for higher resolution scanning, utilizing either a Nikon Plan Fluor 40x 1.3 NA oil objective with  
686 1 um z-slice sectioning or a Nikon Plan Apo Lambda 100x 1.45 NA oil objective with 0.13 um z-slice  
687 sectioning, this ensured that the whole thickness of the tissue would be imaged. Images were saved  
688 on a computer for further processing using custom Fiji/Image J macros<sup>55</sup>.

689

690 **Targeted transcriptomic analysis of specific areas of interest with matched IMC staining and**  
691 **analyses**

692

693 We extracted the RNA sequence data from AOIs (n=46) in three COVID lung sections as described in  
694 our previous paper (Cross, A.R. et al 2022) and organised these into enhanced histopathology

695 classification as described in this paper – ALV, DAD and OP. We then compiled the differential  
696 expressed gene list between the three states (using DESeq2) and performed a pathway analysis using  
697 Reactome<sup>57</sup> (Supplementary Fig. 11). Here, we found upregulation of genes associated with  
698 neutrophil activation when comparing DAD to OP and ALV as observed in Cross A.R. et al. In particular,  
699 S100A8 (highly expressed in neutrophils and a feature of degranulation) and CXCL10 (chemokine  
700 related to neutrophils trafficking) were highly upregulated, supporting trafficking of neutrophil to the  
701 tissue at the DAD phase<sup>58</sup>. High expression of CXCL9 a key chemokine in T cell extravasation into tissue  
702 supports finding of T cells (e.g. CD8 T cells) in these AOIs.

703

704

705 **Data analysis**

706 **Software and algorithms**

707 All software and algorithms used are documented in Table 1.

708

709 **The Spatial Omics Oxford (SpOOx) Analysis Pipeline**

710

711 The SpOOx pipeline is a computational framework that brings together the methods we have used to  
712 derive final spatial interpretation for the COVID-19 lung sections. It incorporates a suite of Python and  
713 R based command line tools which may be run individually or as a semi-automated pipeline. We have  
714 implemented SpOOx using the Ruffus framework<sup>59</sup>. Ruffus allows encapsulation of the workflow and  
715 parameters to enable reproducibility, transparency and code reuse. All steps discussed in the Methods  
716 are encapsulated in the SpOOx pipeline and example commands to achieve the step are shown below.  
717 An overview of the pipeline can be found in Fig. 1a and Supplementary Fig. 1. Full detailed  
718 documentation and a tutorial are included on the SpOOx GitHub page (<https://github.com/Taylor-CCB-Group/SpOOx>). SpOOx produces a series of output directories and files that may be uploaded to  
719 the Multi-Dimensional Viewer (MDV) software (see below). MDV has been developed based on the  
720 Multi Locus View<sup>60</sup> framework and has been heavily modified and extended to allow visualisation and  
721 analysis of large multidimensional data sets, images and the resulting spatial statistics. The code to  
722 upload data to MDV is available on GitHub at <https://github.com/Taylor-CCB-Group/MDV>. Both the  
723 SpOOx and MDV are open source under the GPL 3.0 license with these links – SpOOx is available for  
724 install at <https://github.com/Taylor-CCB-Group/SpOOx> and MDV at <https://github.com/Taylor-CCB-Group/MDV>. The project data analysis is available online within MDV at  
725 <https://mdv.molbiol.ox.ac.uk/projects/hyperion/6567>.

726

727

728

729 **Conversion of MCD files to TIFF.** MCD files were checked for problems with ablation or staining  
730 using the MCD viewer (provided by Standard BioTools). Once these initial checks were  
731 completed, the images were converted to OME-TIFF format for segmentation.

732

733 *Commands: python hyperion\_pipeline.py make mcd\_to\_tiff and python hyperion\_pipeline.py make*  
734 *tiff\_to\_histocat*

735

736 **Segmentation and cell mask generation** Cell segmentation was performed with the Mesmer library  
737 in DeepCell <sup>61</sup>, Nuclear markers (DNA1 and DNA3) and cytoplasmic markers (a-SMA, CCR2, CCR6,  
738 CD107a, CD10, CD114, CD115, CD14, CD15, CD16, CD172a, CD31, CD3, CD45, CD45RO, CD4, CD71,  
739 CD8a, Collagen1, DAP12, EpCAM, GZB, HLA DR, IFN- $\beta$ , IFN- $\gamma$ , PAI1, PanCK, PF4 and RAGE) were  
740 extracted to TIFF files and Z projected to single channel nuclear and cytoplasmic single TIFF images (  
741 Supplementary Fig. 13). These images were contrast adjusted (--contrast 5) and passed to the Mesmer  
742 library (pixel size adjusted to 1 micron) as nuclear and cytoplasm channels. From these, cell  
743 segmentation masks were generated for each ROI.

744

745 *Command: python hyperion\_pipeline.py make deepcell*

746

747

748 **Extraction of signal intensities for each cell.** The intensity of each marker within each labelled cell was  
749 extracted from the data using the segmentation masks using the mean arcsinh-transformed (with –  
750 cofactor 5) pixel intensity for each. The data were recorded as a table, each row representing a cell  
751 with a unique id for the ROI). Shape features such as area, perimeter, eccentricity, and centroid were  
752 also extracted from the masks. All cells were then filtered using a cell area greater than 50  $\mu\text{m}$  and  
753 less than 300  $\mu\text{m}$  to exclude poorly segmented cells and cell debris. Further QC was performed within  
754 MDV by plotting the distribution of marker intensity across each ROI.

755

756 *Command: python hyperion\_pipeline.py make signal\_extraction*

757

758 **Dimensionality reduction and cluster analysis.** For all downstream analysis the intensity values were  
759 arcsinh transformed with a cofactor 5. Clustering was performed using the Phenograph algorithm <sup>62</sup>  
760 through the implementation of the Rphenograph R package (version 0.99.1) with parameter k=30.  
761 Using MDV, the clusters were first visualised using interactive UMAP scatter plots and heatmaps  
762 (showing the median marker intensities per cluster) then manually annotated to define the cell

763 phenotypes at the cell level. The clustering was performed at two levels: a sample level (on the  
764 trimmed [q=0.001] and scaled values) and per condition after having integrated the data with  
765 Harmony (version 1.0)<sup>63</sup>, using the default parameters with the option do\_pca = TRUE. The integration  
766 of the data was performed per condition to remove variation from different patients and to better  
767 define common populations of cells. The annotations before and after integration were compared to  
768 ensure that no biologically meaningful populations were missed when integrating the data. The  
769 heatmaps, PCA and UMAP plots were done using the functions from the CATALYST R package (version  
770 1.16.0).

771

772 *Command: python hyperion\_pipeline.py make phenoharmonycluster.*

773

774 **Annotation workflow.** Cells were first examined for antibody staining and those cells that did not  
775 show any antibody staining were filtered from further analysis. The remaining cells were grouped into  
776 three mega-clusters termed Structural, Myeloid or Lymphocyte based on presence and/or absence of  
777 CD45, EPCAM, PanCK, CD31,  $\alpha$ -SMA, CD56, V $\alpha$ 7.2, CD3, CD14, CD68, PF4 and CD15 expression. The  
778 three mega-clusters were then re-clustered using protein markers selected on immunological basis  
779 (Supplementary Fig. 7). The resultant final clusters were annotated using an integrated approach. In  
780 the first step, we defined clusters using (i) heatmaps showing median marker expression (ii) expression  
781 density histograms which allow better delineation of the range of marker expression, specifically  
782 differentiating low and negative expression levels and (iii) cluster distribution plots which showed the  
783 frequency of each cluster in different samples. Phenotypic similarity of clusters was interrogated via  
784 UMAP and cluster dendrograms. To further define cluster identities, the spatial location of clusters  
785 was visualised using cell centroid plots and mapped onto an adjacent H&E slide with the same ROI.  
786 Based on these analyses, some clusters were excluded under the following criteria: a) clusters with  
787 uniformly low/negative expression of markers, b) clusters only found in one sample, and c) Undefined  
788 clusters (where the combination of markers did not amount to a subset which could be defined). These  
789 clusters were not submitted for spatial analysis. Sub-clusters with very similar expression profiles were  
790 merged and those which contained 2 or more clusters were annotated as such. A small number of  
791 clusters demonstrated expression of markers normally associated with disparate cell populations (e.g.  
792 Neutrophil\_CD8 adjacent), which can be attributed to closely apposed cell types. These adjacent cell  
793 populations were validated via high resolution immunofluorescence microscopy. To aid final  
794 annotation, we also performed Pseudotime inference for selected populations.

795

796 Final annotated clusters were then sense-checked against the MCD images by an independent  
797 investigator not involved in annotating the clusters, and some key clusters of interest were further  
798 examined by immunofluorescence staining with confocal microscopy.

799

800 **Pseudotime analysis.** The Pseudotime analysis was performed on the macrophage, monocytes and  
801 neutrophils populations (Supplementary Fig. 6). Their arcsinh transformed values were integrated  
802 using Harmony with the same parameters as in the main analysis, followed by dimensionality  
803 reduction using UMAP. Then the Pseudotime inference was performed by applying the Slingshot  
804 algorithm<sup>64</sup> to the UMAP dimensions using the default parameters and the above annotations as  
805 clusterLabels.

806

807 This analysis is not part of the SpOOx pipeline but code is available in GitHub.

808 *Command: R slingshot.R <parameters>*

809

810 **Differential cell abundance analysis.** Differential abundance analysis between conditions was  
811 performed using code from the diffcyt R package (version 1.8.8) with the option testDA\_edgeR. To  
812 account for the differences in area between the ablated samples, the area was used as a normalising  
813 factor. The dispersion was estimated using the option trend.method="none" and the negative  
814 binomial generalized log-linear model was used for the analysis (with the glmFit and glmLRT  
815 functions). The BH (Benjamini-Hochberg) method was used to adjust p-values for multiple testing.

816

817 **Cell centroid maps.** For each ROI, the cell centroids were plotted and coloured according to cell type  
818 to produce a cell centroid map which forms the basis of subsequent analyses. These were overlaid  
819 with ROI images in MDV so cell types may be located by colour.

820

## 821 **Spatial analyses**

822

823 A suite of mathematical tools for spatial analyses is incorporated in SpOOx (see below under QCM,  
824 cross-PCF and ACN). The following command runs all the spatial analysis methods in SpOOx:

825

826 *Command: python hyperion\_pipeline.py make spatialstats*

827

828 It is also possible to run each spatial function separately and to adjust parameters (see  
829 <https://github.com/Taylor-CCB-Group/SpOOx/tree/main/src/spatialstats> for details). The command



830 line option that can be appended to the basic command above is stated after each method is  
 831 described.

832

833 **Quadrat Correlation Matrix (QCM).** The “Quadrat Correlation Matrix” (QCM) describes correlations  
 834 between counts of different cell types within square quadrats with edge length 100 $\mu$ m (resulting in  
 835 between 100 and 400 quadrats per ROI), following an approach used by <sup>38</sup> to identify statistically  
 836 significant co-occurrences ( $p < 0.05$ ) and applied to multiplex images of cancer by <sup>65</sup>.

837 We construct the QCM by first generating a matrix  $\mathbf{O}$  whose entries  $O_{ij}$  record the number of cells of  
 838 type  $i$  in quadrat  $j$ , for  $1 \leq i \leq n$  and  $1 \leq j \leq m$ , where  $n$  is the number of cell types in the ROI and  
 839  $m$  is the number of quadrats. We use  $\mathbf{O}$  to generate 1000 matrices  $\mathbf{N}^1, \dots, \mathbf{N}^{1000}$  which form a  
 840 distribution of “observations” in which the number of cells of each type and the number of cells in  
 841 each quadrat are the same as in  $\mathbf{O}$ , but spatial correlations between cell types are removed by shuffling  
 842 cell labels. Each matrix  $\mathbf{N}^k$  is such that, for each  $j$ :

$$\sum_i N_{ij}^k = \sum_i O_{ij}, \quad (1)$$

843 and for each  $i$ :

$$\sum_j N_{ij}^k = \sum_j O_{ij}, \quad (2)$$

844 We construct each matrix  $\mathbf{N}^k$  as follows. We fix  $\mathbf{N}^{k,0} = \mathbf{O}$ , and define rules which permute the entries  
 845 of  $\mathbf{N}^{k,s}$  to obtain a new matrix  $\mathbf{N}^{k,s+1}$ . This is accomplished by selecting two rows  $(a,b)$  and two  
 846 columns  $(c,d)$  of  $\mathbf{N}^{k,s}$  at random. For some integer  $p$  sampled uniformly at random from the interval  
 847  $[0, \min(N_{bc}^{k,s}, N_{ad}^{k,s})]$ , we then fix:

$$N_{ac}^{k,s+1} = N_{ac}^{k,s} + p, \quad (3)$$

$$N_{bc}^{k,s+1} = N_{bc}^{k,s} - p \quad (4)$$

$$N_{bd}^{k,s+1} = N_{bd}^{k,s} + p \quad (5)$$

848 and

$$N_{ad}^{k,s+1} = N_{ad}^{k,s} - p. \quad (6)$$

849 This process is repeated for  $s = 0, 1, \dots, 10,000$  to ensure that the final matrix  $\mathbf{N}^k = \mathbf{N}^{k,10000}$  is well  
 850 shuffled.

851

852 Partial correlation matrices  $\mathbf{C}_O$  and  $\mathbf{C}_{N^1} \dots \mathbf{C}_{N^{1000}}$  are then calculated for  $\mathbf{O}$  and  $N^1, \dots, N^{1000}$   
853 respectively. Standard effect sizes (SES) are determined by rescaling the partial correlations in  $\mathbf{C}_O$  by  
854 the element-wise mean  $\mu$  and standard deviation  $\sigma$  of the  $\mathbf{C}_{N^k}$ , such that

$$SES_{ij} = (\mathbf{C}_{O_{ij}} - \mu [\mathbf{C}_{N^k}]_{ij}) / (\sigma [\mathbf{C}_{N^k}]_{ij}). \quad (7)$$

855

856 Non-significant associations are identified by calculating a 2-tailed p-value for each pair of cell types  
857 and applying a Benjamini-Hochberg correction, with false discovery rate FDR = 0.05. Non-significant  
858 entries of SES are set to 0 in order to generate the QCM, a cell association matrix whose non-zero  
859 entries identify standardised effect sizes of pairs of cell types that are statistically significantly  
860 correlated within the ROI.

861

862 The average QCM across  $Q$  ROIs is obtained by concatenating the relevant observation matrices.  
863 Denoting by  $\mathbf{O}_q$  the observation matrix from ROI  $q$ , we concatenate  $\mathbf{O}_1, \dots, \mathbf{O}_Q$  to form a combined  
864 observation matrix  $\mathbf{O} = (\mathbf{O}_1 \ \mathbf{O}_2 \ \dots \ \mathbf{O}_Q)$ , an  $(n \times (m_1 + m_2 + \dots + m_Q))$  matrix, where  $m_q$  denotes the  
865 number of quadrats in ROI  $q$ . Similarly, we concatenate  $\mathbf{N}_1^k, \dots, \mathbf{N}_Q^k$  to form  $\mathbf{N}^k = (\mathbf{N}_1^k \ \mathbf{N}_2^k \ \dots \ \mathbf{N}_Q^k)$ .  
866 Standard partial correlation matrices are then calculated and then the process described above for a  
867 single ROI is used to compute the average QCM for multiple ROIs.

868

869 *Command option: --function morueta-holme*

870

871 **Cross pair correlation functions (cross-PCF).** Significant correlations identified at length scales in the  
872 range 0-100 $\mu\text{m}$  via the QCM are further assessed by using cross pair correlation functions (cross-PCFs  
873 – see, e.g., Bull 2020). Cross-PCFs quantify clustering and dispersal of pairs of cell populations across  
874 a range of length scales (here 0-300 $\mu\text{m}$ ). The cross-PCF considers pairs of cells which are separated by  
875 distances  $r \in [r_k, r_{k+1})$ , where  $r_0 = 0$  and  $r_k = r_{k-1} + 10$  for  $k = 1, \dots, 30$ .

876

877 For cell populations A and B, the cross-PCF,  $g(r_k)$ , is defined as follows:

$$g(r_k) = \frac{1}{N_A} \sum_{a=1}^{N_A} \sum_{b=1}^{N_B} \frac{I_{[r_k, r_{k+1})}(|x_a - x_b|)}{\rho_{BA, r_k}(x_a)}, \quad (8)$$

878 where  $N_A$  and  $N_B$  are the numbers of cells of types A and B,  $A_{r_k}(\mathbf{x})$  is the area of that portion of an  
879 annulus centred at  $\mathbf{x} = (x, y)$  with inner radius  $r_k$  and outer radius  $r_{k+1}$  which falls within the ROI,  $x_a$   
880 and  $x_b$  are the spatial coordinates of cells  $a$  and  $b$  (of types A and B respectively),  $I_{[r_k, r_{k+1})}(r)$  is an

881 indicator function ( $I_{[r_k, r_{k+1})}(r) = 1$  if  $r \in [r_k, r_{k+1})$  and  $I_{[r_k, r_{k+1})}(r) = 0$  otherwise), and  $\rho_B$  is the  
 882 density of cells of type B in the ROI.

883

884 A cross-PCF with  $g(r) > 1$  means that cells of type A are observed more frequently at distance  $r$  from  
 885 cells of type B than would be expected under complete spatial randomness (CSR), and is indicative of  
 886 clustering at distance  $r$ . Conversely, a cross-PCF with  $g(r) < 1$  means that cells of type A are observed  
 887 less frequently at distance  $r$  from cells of type B than would be expected under CSR, and is indicative  
 888 of exclusion.

889

890 For individual ROIs, 95% confidence intervals are obtained via bootstrapping. The spatial dependence  
 891 of resampled points is accounted for by resampling grid sites within a  $20\mu\text{m}$  square lattice, following  
 892 <sup>66</sup>.

893

894 To aid comparison between the clustering and dispersal of different pairs of cell populations, we  
 895 frequently report cross-PCF values at  $r_k = 20$ , corresponding to length scales in the range  $r \in [20, 30)$   
 896  $\mu\text{m}$ . We focus on  $r_k = 20$  since it approximates the distance between the centroids of cells which are  
 897 in physical contact. For notational simplicity, we denote this value as  $g(r = 20)$ .

898

899 *Command option: --function paircorrelationfunction*

900

901 **Topographical Correlation Map.** The cross-PCF quantifies clustering and dispersal of pairs of cell  
 902 populations at different length scales within an ROI. We also introduce the Topographical Correlation  
 903 Map (TCM), to visualise how the spatial correlation between cells of types A and B, say, changes across  
 904 an ROI.

905

906 In order to define  $\Gamma_{ab}$ , the TCM for cells of types A and B, we first associate a mark  $m_{ab}$  with each cell  
 907  $a$  of type A. The mark  $m_{ab}$  is defined to be the ratio of  $b$ , the number of cells of type B within  $100\mu\text{m}$   
 908 of cell  $a$ , to the expected number of cells of type B if they were distributed according to CSR:

$$m_{ab} = \sum_{j=1}^{N_B} \frac{I_{[0,100)}(|\mathbf{x}_a - \mathbf{x}_j|)}{\rho_B A_{100}(\mathbf{x}_a)}, \quad (9)$$

909 where  $\rho_B$  is the density of cells of type B in the ROI,  $A_{100}(\mathbf{x}_a)$  is the area of that portion of a circle  
 910 with radius  $100\mu\text{m}$  centred at  $\mathbf{x}_a = (x_a, y_a)$  which falls within the ROI,  $I_{[0,100)}(r)$  is an indicator  
 911 function ( $I_{[0,100)}(r) = 1$  when  $0 \leq r < 100$  and  $I_{[0,100)}(r) = 0$  otherwise), and  $N_B$  is the total  
 912 number of cells of type B within the ROI. We interpret values of  $m_{ab}$  in a manner similar to that used

913 for cross-PCFs:  $m_{ab} < 1$  indicates anti-correlation between cells of types A and B within a distance of  
 914  $100\mu\text{m}$ , and  $m_{ab} > 1$  indicates correlation.

915

916 To facilitate visualization and interpretation, we normalize the mark  $m_{ab}$  by introducing the  
 917 transformed mark,  $M_{ab}$ , where:

$$M_{ab}(m_{ab}) = 1 \quad \text{if } m_{ab} \geq \alpha, \quad (10)$$

$$M_{ab}(m_{ab}) = \frac{m_{ab} - 1}{\alpha - 1} \quad \text{if } 1 < m_{ab} \leq \alpha, \quad (11)$$

$$M_{ab}(m_{ab}) = \frac{1 - \frac{1}{m_{ab}}}{\alpha - 1} \quad \text{if } \frac{1}{\alpha} < m_{ab} < 1, \quad (12)$$

$$M_{ab}(m_{ab}) = -1 \quad \text{if } m_{ab} \leq 1/\alpha. \quad (13)$$

918 The constant  $\alpha$  defines a threshold for extreme clustering. If  $m_{ab} > \alpha$  then we have strong clustering  
 919 and we fix  $M_{ab} = 1$ ; if  $m_{ab} \leq 1/\alpha$  then we have strong exclusion and we fix  $M_{ab} = -1$ .  
 920 A sketch of  $M_{ab}$  is presented in Supplementary Fig. 14.

921

922 We note the following properties of the transformed mark,  $M_{ab}$ . First,  $M_{ab}(m_{ab}) = -M_{ab}(\frac{1}{m_{ab}})$ , so  
 923 that dispersal and clustering are measured on the same scales. For example,  $m_{ab} = 2$  indicates the  
 924 presence of twice as many cells of type B as expected under CSR, while  $m_{ab} = 1/2$  indicates the  
 925 presence of half as many cells of type B as expected under CSR. Secondly, the magnitude of  $M_{ab}$   
 926 describes the strength of the spatial interaction. Finally, the sign of  $M_{ab}$  identifies whether there is  
 927 clustering ( $M_{ab} > 0$ ) or exclusion ( $M_{ab} < 0$ ) between cell  $a$  (of type A) and cells of type B.

928

929 The parameter  $\alpha$  characterises the most extreme clustering or exclusion which can be resolved in each  
 930 kernel, with extremal values being mapped to 1 and -1 respectively. We use  $\alpha = 5$ , so clustering or  
 931 exclusion stronger than 5x is interpreted as the strongest clustering/exclusion that we can distinguish.

932

933 After calculating  $M_{ab}$  for each cell of type  $a$  across the ROI, we centre a Gaussian kernel, with standard  
 934 deviation  $\sigma = 50\mu\text{m}$ , and maximum height  $M_{ab}$ , at  $\mathbf{x}_a$ . We sum the kernels associated with all cells  
 935 of type A to generate the TCM,  $\Gamma_{ab}(\mathbf{x})$ :

$$\Gamma_{ab}(\mathbf{x}) = \sum_{a=1}^{N_A} \frac{M_{ab}}{\sigma\sqrt{2\pi}} e^{-\frac{1}{2\sigma^2}|\mathbf{x}-\mathbf{x}_a|^2}. \quad (14)$$

936

937 The TCM permits identification of spatial locations in which cells of type A are positively ( $\Gamma_{ab} \gg 0$ ) or  
938 negatively ( $\Gamma_{ab} \ll 0$ ) associated with cells of type B. For computational efficiency, when calculating  
939  $\Gamma_{ab}$ , we assume that each kernel has compact support, being centred in a square region of edge length  
940  $300\mu\text{m}$ .

941

942 Finally, we note that  $\Gamma_{ab} \neq \Gamma_{ba}$ , since the kernels used to construct  $\Gamma_{ab}$  are centered on cells of type  
943 A (and vice versa). While areas in which cells of type A and type B are co-located should be identified  
944 by both  $\Gamma_{ab}$  and  $\Gamma_{ba}$ , their values will differ in regions rich in one cell type and poor in another. We  
945 therefore stress that  $\Gamma_{ab}$  describes locations in which cells of type A are correlated or anti-correlated  
946 with cells of type B, and that the presence or absence of cells of type B cannot be inferred from regions  
947 in which  $\Gamma_{ab}$  is close to 0.

948

949 *Command option: --function localclusteringheatmaps*

950

951 **Adjacency Cell Networks.** We use the cell segmentation masks generated by DeepCell to produce a  
952 spatially-embedded adjacency cell network (ACN), whose nodes represent cell centres and are  
953 labelled according to their cell type. Nodes are connected by an edge if the corresponding cells in the  
954 segmentation mask share a border. To ensure that small perturbations in cell boundaries do not lead  
955 to errors in cell connections, we expand the border of each segmented cell by 5 pixels before  
956 generating the network.

957

958 We use the ACN to define two statistics for each pairwise combination of cell types A and B. First, we  
959 compute  $\phi_{AB}$ , the proportion of cells of type A which are in contact with at least one cell of type B:

$$\phi_{AB} = \frac{1}{N_A} \sum_{a=1}^{N_A} I_B(a), \quad (15)$$

960 where  $N_A$  is the number of cells of type A and  $I_B(a)$  is an indicator function ( $I_B(a) = 1$  if cell  $a$  is  
961 connected with a cell of type B and  $I_B(a) = 0$  otherwise). Secondly, we calculate  $\Phi_{AB}$ , the average  
962 number of cells of type B that are in contact with a cell of type A:

$$\Phi_{AB} = \frac{1}{N_A} \sum_{a=1}^{N_A} \eta_B(a), \quad (16)$$

963 where  $\eta_B(a)$  is the number of cells of type B in contact with cell  $a$ .

964

965 In this paper, we used the ACN to calculate  $\phi_{AB}$ , the proportion of cells of type A that have at least  
966 one cell of type B in contact with them, and  $\Phi_{AB}$ , the average number of cells of type B that are in  
967 contact with a cell of type A in the ROI.

968

969 *Command option: --function networkstatistics*

970

## 971 **Multi-Dimensional Viewer (MDV)**

972

973 MDV is a comprehensive spatial analytics platform that facilitates the interrogation of large complex  
974 data sets and includes various interactive dashboards to facilitate quality control, interactive  
975 clustering, phenotyping and spatial analysis. It is an open source web application which can be  
976 downloaded and installed locally or used on the publicly available web site  
977 <http://mdv.molbiol.ox.ac.uk>. Users register to use the site and projects can private, shared with other  
978 users or made public. Full documentation and tutorial videos are provided on the MDV website but  
979 we provide an overview here.

980

981 MDV allows output generated by the SpOOx pipeline to be loaded at different states. Data locations  
982 are specified in a yaml format file which can be edited by the user (command: `python mdvupload.py`  
983 `myconfig.yaml`). Examples of data tables that may be uploaded are:

984

- 985 ● Image data (PNGs/OME-TIFF stacks): ROI image stacks, H and E images binary cell  
986 masks.
- 987 ● Cell data (tab separated file): one cell per row, including size, size, shape, phenograph  
988 clusters identification, UMAP coordinates, marker signal intensities.
- 989 ● Spatial Statistics data (tab separated file): one row containing cell to cell interaction  
990 data and associated statistics.
- 991 ● Data related to the disease states (JSON file): allowing grouping of samples for high  
992 level analysis.

993

994 Once uploaded the data are presented in MDV as a series of views that contain multiple interactive  
995 charts corresponding to different analytical methods from clustering, annotation, cell centroid  
996 visualisation and spatial analytical methods. Each view focuses on a particular aspect of the pipeline.  
997 View contents can be adjusted and added to by adding other chart types and saved as a new view.  
998 Chart types can be D3 components ( <https://d3js.org/> ) but we have also written custom chart types

999 for performance reasons. For example, MDV scatterplot chart can visualise and interrogate at least 10  
1000 million data points. We also integrate Viv viewer<sup>67</sup> to visualise composite image stacks.

1001

1002 The complete analysis and data set were published by publicly sharing the data at

1003 <https://mdv.molbiol.ox.ac.uk/projects/hyperion/6356>.

1004

#### 1005 **COMBAT data mapping**

1006

1007 **COMBAT CyTOF data generation and processing.** Cell suspension mass cytometry (CyTOF) data were  
1008 generated by the COMBAT consortium as previously described<sup>6</sup>. In brief, whole blood from COVID-19  
1009 patients was stabilised using a Cytodelics fixative solution, red blood cells were lysed, cellular material  
1010 was fixed, and samples were run in a Helios CyTOF machine. Importantly, samples were enriched for  
1011 mononuclear cells before profiling by performing magnetic depletion of CD66<sup>+</sup> granulocytes.

1012

1013 After acquisition, data were formatted into a single-cell protein abundance table and annotated into  
1014 cell types based on marker expression<sup>6</sup>. For the analyses in the present study, this expression matrix  
1015 was split into two subsets: one containing T and NK cell types, and a second one containing myeloid  
1016 cell types (i.e. monocyte subsets).

1017

1018 **Mapping cells from lung tissue to blood cells from the COMBAT study<sup>6</sup>.** Cells in the lung dataset were  
1019 matched to the most closely related cell types in blood using scmap, a method which enables label  
1020 projection by calculating the similarity between cells profiled by two separate studies<sup>33</sup>. In brief,  
1021 CyTOF and CITE-seq expression matrices from the COMBAT study were used to build index references  
1022 for label projection. First, proteins which were detected in both studies were identified. This resulted  
1023 in a panel of 13 and 18 proteins shared between our study and the COMBAT CyTOF and CITE-seq  
1024 panels, respectively. Next, these proteins were used as a basis for cell type classification with the  
1025 scmapCluster function. Classification accuracy was tested by splitting the COMBAT data into training  
1026 and test sets containing 80% and 20% of cells, respectively. The training set was used to generate the  
1027 scmap reference index, while the test set was used to assess cell type prediction accuracy<sup>33</sup>. Given  
1028 the reduced set of markers shared between studies, not all COMBAT cell populations could be  
1029 accurately predicted. Thus, in order to maximise predictive accuracy similar subpopulations of the  
1030 same cell type were merged into a single group and any cell types known to be absent from our lung  
1031 data, such as B cells and plasmablasts, were removed. This approach achieved over 70% accuracy for  
1032 CyTOF data (71% and 78% predictive accuracy for myeloid and lymphoid cell types, respectively) and

1033 85% accuracy for CITE-seq data and components of final merged clusters are shown in Supplementary  
1034 Fig. 16.

1035

1036 Indexed references were next used to match cells in the lung to the most similar clusters in blood  
1037 using the scmapCluster() function. To do so, cell type labels were predicted for each cell in the lung  
1038 based on the CyTOF and CITE-seq reference sets. Any unassigned cells were discarded. Cluster overlap  
1039 between studies was visualised using Sankey diagrams<sup>68</sup> and quantified using Jaccard indexes<sup>69</sup>.

1040

1041 **Neutrophil subset analysis from stored COMBAT samples.** Whole blood samples frozen in whole  
1042 blood cell stabilizer (Cytodelics) were obtained from COMBAT consortium storage for healthy  
1043 volunteers (n=11), health care workers (n=12), COVID-19 (n=93) and Sepsis (n=48). Pre-processed  
1044 CD45<sup>+</sup> gated FCS files of granulocyte containing whole blood samples were analysed with R (v4.0.0).  
1045 50000 cells per sample were integrated using Harmony (v1.0)<sup>2</sup> and the CATALYST package  
1046 (v1.14.0)<sup>3</sup> was used for downstream analysis. CD45<sup>+</sup> cells were clustered based on the FlowSOM and  
1047 ConsensusClusterPlus algorithms using the cluster () function. 50 metaclusters (xdim=100, ydim=100,  
1048 k=50) were then assigned to major cell types (T cells, B cells, plasmablasts, mononuclear phagocytes  
1049 and neutrophils). Neutrophils were selected and reclustered based on CD45, CD15, CD38, CD64, CD16,  
1050 CD43, CD66b CD10, CD33, KI67, CD172a/b, CD141, CD71, CD114, CD371 and CD274 expression. 30  
1051 neutrophil metaclusters (xdim=100, ydim=100, k=30) were manually merged to 8 neutrophil clusters  
1052 (proNeut, preNeut, iNeut1-3, mNeut1-3) based on median marker expression.

1053

#### 1054 **Data availability**

1055 The spatial mass cytometry dataset (MCD) files and results of analysis by the Spatial Omics Oxford  
1056 pipeline are available at <https://doi.org/10.5281/zenodo.6513508>. The analysis results are also  
1057 presented as a dynamic online resource in Multi-Dimensional Viewer (MDV)  
1058 (<https://mdv.molbiol.ox.ac.uk/projects/hyperion/6567>). All source data are found in  
1059 <https://doi.org/10.5281/zenodo.6513508>; and also within the hyperion 6567 project in the MDV link.  
1060 Specific source data for graphs are also provided in Source Data File. Source data are provided with  
1061 this paper.

1062

#### 1063 **Code availability**

1064 The complete code for the Spatial Omics Oxford pipeline is available as a GitHub repository under  
1065 the GPL license: <https://github.com/Taylor-CCB-Group/SpOOx>. In addition, the SpOOx pipeline has  
1066 been deposited at Zenodo (<https://zenodo.org/record/8320986>). The Multi-Dimensional Viewer



1067 code is available under the GPL license: <https://github.com/Taylor-CCB-Group/MDV>. This package  
1068 has also been deposited at Zenodo (<https://zenodo.org/record/8324918>).  
1069

1070 **References**

1071

- 1072 1 Wang et al. Estimating excess mortality due to the COVID-19 pandemic: a systematic analysis  
1073 of COVID-19-related mortality, 2020-21. *Lancet* **399**, 1513-1536 (2022).  
1074 [https://doi.org:10.1016/S0140-6736\(21\)02796-3](https://doi.org:10.1016/S0140-6736(21)02796-3)
- 1075 2 Gorog, D. A. et al. Current and novel biomarkers of thrombotic risk in COVID-19: a Consensus  
1076 Statement from the International COVID-19 Thrombosis Biomarkers Colloquium. *Nat Rev*  
1077 *Cardiol* **19**, 475-495 (2022). <https://doi.org:10.1038/s41569-021-00665-7>
- 1078 3 Lamers, M. M. & Haagmans, B. L. SARS-CoV-2 pathogenesis. *Nat Rev Microbiol* **20**, 270-284  
1079 (2022). <https://doi.org:10.1038/s41579-022-00713-0>
- 1080 4 Nalbandian, A. et al. Post-acute COVID-19 syndrome. *Nat Med* **27**, 601-615 (2021).  
1081 <https://doi.org:10.1038/s41591-021-01283-z>
- 1082 5 Pustake, M., Tambolkar, I., Giri, P. & Gandhi, C. SARS, MERS and CoVID-19: An overview and  
1083 comparison of clinical, laboratory and radiological features. *J Family Med Prim Care* **11**, 10-17  
1084 (2022). <https://doi.org:10.4103/jfmprc.jfmprc.839.21>
- 1085 6 COMBAT. A blood atlas of COVID-19 defines hallmarks of disease severity and specificity. *Cell*  
1086 **185**, 916-938 e958 (2022). <https://doi.org:10.1016/j.cell.2022.01.012>
- 1087 7 Kusnadi, A. et al. Severely ill COVID-19 patients display impaired exhaustion features in SARS-  
1088 CoV-2-reactive CD8(+) T cells. *Sci Immunol* **6** (2021).  
1089 <https://doi.org:10.1126/sciimmunol.abe4782>
- 1090 8 Mann, E. R. et al. Longitudinal immune profiling reveals key myeloid signatures associated  
1091 with COVID-19. *Sci Immunol* **5** (2020). <https://doi.org:10.1126/sciimmunol.abd6197>
- 1092 9 Schulte-Schrepping, J. et al. Severe COVID-19 Is Marked by a Dysregulated Myeloid Cell  
1093 Compartment. *Cell* **182**, 1419-1440 e1423 (2020). <https://doi.org:10.1016/j.cell.2020.08.001>
- 1094 10 Unterman, A. et al. Single-cell multi-omics reveals dyssynchrony of the innate and adaptive  
1095 immune system in progressive COVID-19. *Nature Communications* **13**, 440 (2022).  
1096 <https://doi.org:10.1038/s41467-021-27716-4>
- 1097 11 Wang, X. et al. Dysregulated hematopoiesis in bone marrow marks severe COVID-19. *Cell*  
1098 *Discovery* **7**, 60 (2021). <https://doi.org:10.1038/s41421-021-00296-9>
- 1099 12 Chen, S. T. et al. A shift in lung macrophage composition is associated with COVID-19 severity  
1100 and recovery. *Science Translational Medicine* **14**, eabn5168  
1101 <https://doi.org:10.1126/scitranslmed.abn5168>
- 1102 13 Wang, S. et al. A single-cell transcriptomic landscape of the lungs of patients with COVID-19.  
1103 *Nature Cell Biology* **23**, 1314-1328 (2021). <https://doi.org:10.1038/s41556-021-00796-6>
- 1104 14 Wendisch, D. et al. SARS-CoV-2 infection triggers profibrotic macrophage responses and lung  
1105 fibrosis. *Cell* **184**, 6243-6261.e6227 (2021). <https://doi.org:10.1016/j.cell.2021.11.033>
- 1106 15 Melms, J. C. et al. A molecular single-cell lung atlas of lethal COVID-19. *Nature* **595**, 114-119  
1107 (2021). <https://doi.org:10.1038/s41586-021-03569-1>
- 1108 16 de Rooij, L. et al. The pulmonary vasculature in lethal COVID-19 and idiopathic pulmonary  
1109 fibrosis at single cell resolution. *Cardiovascular research* (2022).  
1110 <https://doi.org:10.1093/cvr/cvac139>
- 1111 17 Delorey, T. M. et al. COVID-19 tissue atlases reveal SARS-CoV-2 pathology and cellular targets.  
1112 *Nature* **595**, 107-113 (2021). <https://doi.org:10.1038/s41586-021-03570-8>
- 1113 18 Bharat, A. et al. Lung transplantation for patients with severe COVID-19. *Sci Transl Med* **12**  
1114 (2020). <https://doi.org:10.1126/scitranslmed.abe4282>
- 1115 19 Rendeiro, A. F. et al. The spatial landscape of lung pathology during COVID-19 progression.  
1116 *Nature* **593**, 564-569 (2021). <https://doi.org:10.1038/s41586-021-03475-6>
- 1117 20 Melero, I. et al. Neutrophil Extracellular Traps, Local IL-8 Expression, and Cytotoxic T-  
1118 Lymphocyte Response in the Lungs of Patients With Fatal COVID-19. *Chest* **162**, 1006-1016  
1119 (2022). <https://doi.org:10.1016/j.chest.2022.06.007>

1120 21 Carsana, L. *et al.* Pulmonary post-mortem findings in a series of COVID-19 cases from northern  
1121 Italy: a two-centre descriptive study. *The Lancet. Infectious diseases* **20**, 1135-1140 (2020).  
1122 [https://doi.org:10.1016/s1473-3099\(20\)30434-5](https://doi.org:10.1016/s1473-3099(20)30434-5)

1123 22 Youd, E. & Moore, L. COVID-19 autopsy in people who died in community settings: the first  
1124 series. *Journal of clinical pathology* **73**, 840-844 (2020). [https://doi.org:10.1136/iclinpath-](https://doi.org:10.1136/iclinpath-2020-206710)  
1125 [2020-206710](https://doi.org:10.1136/iclinpath-2020-206710)

1126 23 Menter, T. *et al.* Postmortem examination of COVID-19 patients reveals diffuse alveolar  
1127 damage with severe capillary congestion and variegated findings in lungs and other organs  
1128 suggesting vascular dysfunction. *Histopathology* **77**, 198-209 (2020).  
1129 <https://doi.org:10.1111/his.14134>

1130 24 Xu, Z. *et al.* Pathological findings of COVID-19 associated with acute respiratory distress  
1131 syndrome. *The Lancet. Respiratory medicine* **8**, 420-422 (2020).  
1132 [https://doi.org:10.1016/s2213-2600\(20\)30076-x](https://doi.org:10.1016/s2213-2600(20)30076-x)

1133 25 Mauad, T. *et al.* Tracking the time course of pathological patterns of lung injury in severe  
1134 COVID-19. *Respiratory research* **22**, 32 (2021). <https://doi.org:10.1186/s12931-021-01628-9>

1135 26 Angeles Montero-Fernandez, M. & Pardo-Garcia, R. Histopathology features of the lung in  
1136 COVID-19 patients. *Diagnostic histopathology (Oxford, England)* **27**, 123-127 (2021).  
1137 <https://doi.org:10.1016/j.mpdhp.2020.11.009>

1138 27 Borczuk, A. C. *et al.* COVID-19 pulmonary pathology: a multi-institutional autopsy cohort from  
1139 Italy and New York City. *Mod Pathol* **33**, 2156-2168 (2020). [https://doi.org:10.1038/s41379-](https://doi.org:10.1038/s41379-020-00661-1)  
1140 [020-00661-1](https://doi.org:10.1038/s41379-020-00661-1)

1141 28 Vadasz, I. *et al.* Severe organising pneumonia following COVID-19. *Thorax* **76**, 201-204 (2021).  
1142 <https://doi.org:10.1136/thoraxjnl-2020-216088>

1143 29 Greenwald, N. F. *et al.* Whole-cell segmentation of tissue images with human-level  
1144 performance using large-scale data annotation and deep learning. *Nat Biotechnol* **40**, 555-565  
1145 (2022). <https://doi.org:10.1038/s41587-021-01094-0>

1146 30 Barkauskas, C. E. *et al.* Type 2 alveolar cells are stem cells in adult lung. *The Journal of clinical*  
1147 *investigation* **123**, 3025-3036 (2013). <https://doi.org:10.1172/jci68782>

1148 31 Zacharias, W. J. *et al.* Regeneration of the lung alveolus by an evolutionarily conserved  
1149 epithelial progenitor. *Nature* **555**, 251-255 (2018). <https://doi.org:10.1038/nature25786>

1150 32 Choi, J. *et al.* Inflammatory Signals Induce AT2 Cell-Derived Damage-Associated Transient  
1151 Progenitors that Mediate Alveolar Regeneration. *Cell stem cell* **27**, 366-382.e367 (2020).  
1152 <https://doi.org:10.1016/j.stem.2020.06.020>

1153 33 Kiselev, V. Y., Yiu, A. & Hemberg, M. scmap: projection of single-cell RNA-seq data across data  
1154 sets. *Nat Methods* **15**, 359-362 (2018). <https://doi.org:10.1038/nmeth.4644>

1155 34 Zhao, Y. *et al.* High levels of virus-specific CD4+ T cells predict severe pandemic influenza A  
1156 virus infection. *Am J Respir Crit Care Med* **186**, 1292-1297 (2012).  
1157 <https://doi.org:10.1164/rccm.201207-1245OC>

1158 35 Lanzavecchia, A. & Sallusto, F. Understanding the generation and function of memory T cell  
1159 subsets. *Current opinion in immunology* **17**, 326-332 (2005).  
1160 <https://doi.org:10.1016/j.coi.2005.04.010>

1161 36 Baddeley, A. *et al.* On tests of spatial pattern based on simulation envelopes. **84**, 477-489  
1162 (2014). <https://doi.org:https://doi.org/10.1890/13-2042.1>

1163 37 Guseva, K. *et al.* From diversity to complexity: Microbial networks in soils. *Soil Biology and*  
1164 *Biochemistry* **169**, 108604 (2022).  
1165 <https://doi.org:https://doi.org/10.1016/j.soilbio.2022.108604>

1166 38 Morueta-Holme, N. *et al.* A network approach for inferring species associations from co-  
1167 occurrence data. *Ecography* **39**, 1139-1150 (2016). <https://doi.org:10.1111/ecog.01892>

1168 39 Slyper, M. *et al.* Author Correction: A single-cell and single-nucleus RNA-Seq toolbox for fresh  
1169 and frozen human tumors. *Nat Med* **26**, 1307 (2020). [https://doi.org:10.1038/s41591-020-](https://doi.org:10.1038/s41591-020-0976-3)  
1170 [0976-3](https://doi.org:10.1038/s41591-020-0976-3)

1171 40 Governa, V. *et al.* The Interplay Between Neutrophils and CD8(+) T Cells Improves Survival in  
1172 Human Colorectal Cancer. *Clinical cancer research : an official journal of the American*  
1173 *Association for Cancer Research* **23**, 3847-3858 (2017). [https://doi.org:10.1158/1078-](https://doi.org:10.1158/1078-0432.Ccr-16-2047)  
1174 [0432.Ccr-16-2047](https://doi.org:10.1158/1078-0432.Ccr-16-2047)  
1175 41 Schwab, L. *et al.* Neutrophil granulocytes recruited upon translocation of intestinal bacteria  
1176 enhance graft-versus-host disease via tissue damage. *Nat Med* **20**, 648-654 (2014).  
1177 <https://doi.org:10.1038/nm.3517>  
1178 42 Takashima, A. & Yao, Y. Neutrophil plasticity: acquisition of phenotype and functionality of  
1179 antigen-presenting cell. *Journal of leukocyte biology* **98**, 489-496 (2015).  
1180 <https://doi.org:10.1189/jlb.1MR1014-502R>  
1181 43 Samadi, N. *et al.* T-cell-derived cytokines enhance the antigen-presenting capacity of human  
1182 neutrophils. *European Journal of Immunology* **49**, 1441-1443 (2019).  
1183 <https://doi.org:https://doi.org/10.1002/eji.201848057>  
1184 44 Schwabenland, M. *et al.* Deep spatial profiling of human COVID-19 brains reveals  
1185 neuroinflammation with distinct microanatomical microglia-T-cell interactions. *Immunity* **54**,  
1186 1594-1610.e1511 (2021). <https://doi.org:10.1016/j.immuni.2021.06.002>  
1187 45 Liao, M. *et al.* Single-cell landscape of bronchoalveolar immune cells in patients with COVID-  
1188 19. *Nat Med* **26**, 842-844 (2020). <https://doi.org:10.1038/s41591-020-0901-9>  
1189 46 Olajuyin, A. M., Zhang, X. & Ji, H. L. Alveolar type 2 progenitor cells for lung injury repair. *Cell*  
1190 *Death Discov* **5**, 63 (2019). <https://doi.org:10.1038/s41420-019-0147-9>  
1191 47 Bert, S., Nadkarni, S. & Perretti, M. Neutrophil-T cell crosstalk and the control of the host  
1192 inflammatory response. *Immunol Rev* (2022). <https://doi.org:10.1111/imr.13162>  
1193 48 Costa, S., Bevilacqua, D., Cassatella, M. A. & Scapini, P. Recent advances on the crosstalk  
1194 between neutrophils and B or T lymphocytes. *Immunology* **156**, 23-32 (2019).  
1195 <https://doi.org:10.1111/imm.13005>  
1196 49 Ziegler, C. G. K. *et al.* SARS-CoV-2 Receptor ACE2 Is an Interferon-Stimulated Gene in Human  
1197 Airway Epithelial Cells and Is Detected in Specific Cell Subsets across Tissues. *Cell* **181**, 1016-  
1198 1035.e1019 (2020). <https://doi.org:10.1016/j.cell.2020.04.035>  
1199 50 Chua, R. L. *et al.* COVID-19 severity correlates with airway epithelium-immune cell  
1200 interactions identified by single-cell analysis. *Nature Biotechnology* **38**, 970-979 (2020).  
1201 <https://doi.org:10.1038/s41587-020-0602-4>  
1202 51 Rapkiewicz, A. V. *et al.* Megakaryocytes and platelet-fibrin thrombi characterize multi-organ  
1203 thrombosis at autopsy in COVID-19: A case series. *EClinicalMedicine* **24**, 100434 (2020).  
1204 <https://doi.org:10.1016/j.eclinm.2020.100434>  
1205 52 Cross, A. R. *et al.* Spatial transcriptomic characterization of COVID-19 pneumonitis identifies  
1206 immune circuits related to tissue injury. *JCI Insight* (2022).  
1207 <https://doi.org:10.1172/jci.insight.157837>  
1208 53 Recalde-Zamacona, B. *et al.* Histopathological findings in fatal COVID-19 severe acute  
1209 respiratory syndrome: preliminary experience from a series of 10 Spanish patients. *Thorax* **75**,  
1210 1116-1118 (2020). <https://doi.org:10.1136/thoraxjnl-2020-215577>  
1211 54 Bankhead, P. *et al.* QuPath: Open source software for digital pathology image analysis. *Sci Rep*  
1212 **7**, 16878 (2017). <https://doi.org:10.1038/s41598-017-17204-5>  
1213 55 Schindelin, J. *et al.* Fiji: an open-source platform for biological-image analysis. *Nat Methods* **9**,  
1214 676-682 (2012). <https://doi.org:10.1038/nmeth.2019>  
1215 56 Chevrier, S. *et al.* Compensation of Signal Spillover in Suspension and Imaging Mass  
1216 Cytometry. *Cell Syst* **6**, 612-620 e615 (2018). <https://doi.org:10.1016/j.cels.2018.02.010>  
1217 57 Griss, J. *et al.* ReactomeGSA - Efficient Multi-Omics Comparative Pathway Analysis. *Molecular*  
1218 *& cellular proteomics : MCP* **19**, 2115-2125 (2020).  
1219 <https://doi.org:10.1074/mcp.TIR120.002155>

- 1220 58 Ichikawa, A. *et al.* CXCL10-CXCR3 enhances the development of neutrophil-mediated  
1221 fulminant lung injury of viral and nonviral origin. *Am J Respir Crit Care Med* **187**, 65-77 (2013).  
1222 <https://doi.org:10.1164/rccm.201203-0508OC>
- 1223 59 Goodstadt, L. Ruffus: a lightweight Python library for computational pipelines. *Bioinformatics*  
1224 **26**, 2778-2779 (2010). <https://doi.org:10.1093/bioinformatics/btq524>
- 1225 60 Sergeant, M. J. *et al.* Multi Locus View: an extensible web-based tool for the analysis of  
1226 genomic data. *Commun Biol* **4**, 623 (2021). <https://doi.org:10.1038/s42003-021-02097-y>
- 1227 61 Van Valen, D. A. *et al.* Deep Learning Automates the Quantitative Analysis of Individual Cells  
1228 in Live-Cell Imaging Experiments. *PLoS Comput Biol* **12**, e1005177 (2016).  
1229 <https://doi.org:10.1371/journal.pcbi.1005177>
- 1230 62 Levine, J. H. *et al.* Data-Driven Phenotypic Dissection of AML Reveals Progenitor-like Cells that  
1231 Correlate with Prognosis. *Cell* **162**, 184-197 (2015). <https://doi.org:10.1016/j.cell.2015.05.047>
- 1232 63 Korsunsky, I. *et al.* Fast, sensitive and accurate integration of single-cell data with Harmony.  
1233 *Nat Methods* **16**, 1289-1296 (2019). <https://doi.org:10.1038/s41592-019-0619-0>
- 1234 64 Street, K. *et al.* Slingshot: cell lineage and pseudotime inference for single-cell transcriptomics.  
1235 *BMC Genomics* **19**, 477 (2018). <https://doi.org:10.1186/s12864-018-4772-0>
- 1236 65 Prabhakaran S., G. C., Robertson-Tessi M., Beg A. A., Gray J., Antonia S., Gatenby R. A.,  
1237 Anderson A. R. A. Distinct tumor-immune ecologies in NSCLC patients predict progression and  
1238 define a clinical biomarker of therapy response. *bioRxiv preprint* (2022).  
1239 <https://doi.org:doi:10.1101/2022.10.22.513219>
- 1240 66 Loh, J. M. A valid and fast spatial bootstrap for correlation functions. *Astrophys J* **681**, 726-734  
1241 (2008). <https://doi.org:Doi 10.1086/588631>
- 1242 67 Manz, T. *et al.* Viv: multiscale visualization of high-resolution multiplexed bioimaging data on  
1243 the web. *Nat Methods* **19**, 515-516 (2022). <https://doi.org:10.1038/s41592-022-01482-7>
- 1244 68 Schmidt, M. The sankey diagram in energy and material flow management. *J Ind Ecol* **12**, 82-  
1245 94 (2008). <https://doi.org:10.1111/j.1530-9290.2008.00004.x>
- 1246 69 Jaccard, P. The distribution of the flora in the alpine zone. *New Phytol* **11 (2)** (1912).
- 1247 70. Büttner, M., Ostner, J., Müller, C. L., Theis, F. J. & Schubert, B. scCODA is a Bayesian model  
1248 for compositional single-cell data analysis. *Nat. Commun.* 2021 121 **12**, 1–10 (2021).  
1249  
1250

## 1251 Acknowledgements

1252 We thank patients' relatives for donation of the patients' lung tissue. This work was funded by the  
1253 Oxford University Medical Sciences Division COVID Funds, NIHR Oxford Biomedical Research Centre  
1254 and the Chinese Academy of Medical Sciences (CAMS) Innovation Fund for Medical Science (CIFMS),  
1255 China (grant number: 2018-I2M- 2-002). LD and CV are supported by the NIHR Oxford Biomedical  
1256 Research Centre. LPH is supported by MRC Human Immunology Unit (grant (MC\_UU\_00008/1) and  
1257 the NIHR Oxford Biomedical Research Centre (NIHR203311).

## 1258 Author Contributions Statement

1259

1260 PW analysed the data, contributed to development of MDV, spatial analyses, and interpretation of  
1261 mathematical output and all spatial data, and writing of the paper. LD contributed to analysis and  
1262 interpretation of data, optimised and performed the staining of the lung sections in conjunction with

1263 RE, analysed MCD images and contributed to the writing of the paper. JB performed all the  
1264 mathematical development and analysis in conjunction with HB and contributed to interpretation of  
1265 data and writing of the paper. ER performed all bioinformatic analysis and contributed to  
1266 interpretation of data and writing of the paper. CV performed all the immunofluorescence and  
1267 imaging of sections. GDHT and CC performed all the histopathology analyses in conjunction with LPH.  
1268 AC performed the protein immunostaining of the sections and contributed to interpretation of data.  
1269 CEDA and IMB organised acquisition of patient samples, clinical data and ethical permissions. YXZ and  
1270 DA optimised, performed CYTOF experiments on neutrophils and analysed data. ECG and JW  
1271 performed all COSMIC v COMBAT data analysis in conjunction with PW, LPH and JK. DR and PK  
1272 interpreted data, acquired some of the funding for the study and contributed to writing of the paper.  
1273 TD, IAU, GO, CM, JK, FI interpreted data, discussed annotations and immunological analysis, and  
1274 contributed to writing of the paper. DS and SMG performed early code testing for the pipeline. ST  
1275 oversaw all computational work and code writing for the study, contributed to analysis of data and  
1276 writing of paper. MS performed all the dataset organisation and spatial analysis set up in MDV, wrote  
1277 the codes and organised MDV in conjunction with PW, ST, and LPH. JMW, AA, PW and LPH performed  
1278 and analysed all the transcriptomic data from previous studies and publicly deposited data, and  
1279 revisions of paper. HB oversaw all mathematical development and contributed to writing of the paper.  
1280 LPH conceptualized, led the study, acquired funding, analysed the data and wrote the manuscript. All  
1281 authors read and approved the final manuscript.

1282

1283 Our authorship is diverse, inclusive and equal. There is representation from both sexes, high and low  
1284 income countries of origin, age, and minorities.

1285

### 1286 **Competing interests Statement**

1287 PK has acted as a consultant for Biomunex, Infinitopes, Astra Zeneca and UCB. The remaining  
1288 authors declare no competing interests.

1289

1290

1291

1292

1293

1294

1295

1296

1297

1298 **Figure legends**

1299 **Fig. 1. Spatial analysis pipeline and histopathology categorisation of samples**

- 1300 A. Overview of the workflow and SpOOx pipeline. The steps of the analysis are presented in  
1301 Supplementary Fig. 1 in more detail. n=677,623 single cells refer to segmented cells, without  
1302 filtering for cells with no antibody staining, and 'undefined' clusters. IMC – imaging mass  
1303 cytometry.
- 1304 B. H&E section from COVID-19 tissue section showing formal histopathology features of alveolitis  
1305 (ALV), diffuse alveolar damage (DAD) and organizing pneumonia with their corresponding MCD  
1306 file image showing staining for 5 of 35 antibodies ( $\alpha$ -SMA, EpCAM, PanCK, Col 1a and CD31).  
1307 'a'-'c' in figure refer to characteristic features of ALV, DAD and OP. 'a' - thickened alveolar  
1308 epithelial wall and septae with immune cell infiltrate and congestion of alveolar walls 'b'  
1309 widespread presence of hyaline membrane, and regenerating/proliferating Type II alveolar  
1310 epithelium and 'c' -fibroblasts and collagen presence around bronchial epithelium. See also  
1311 Supplementary Fig. 2. Representative H&E and MCD images is for ROI from n=10 ROIs for ALV,  
1312 n=8 ROIs (DAD), n=8 ROIs (OP); n=12 patients. H&E staining performed once per tissue section.  
1313 37-plex staining was performed once for each lung sample.
- 1314 C. Point when samples were obtained from the first day of symptoms and corresponding  
1315 histopathology states in lung sections. Mean and S.D. shown, p value calculated using one-way  
1316 ANOVA test with Tukey's multiple comparison test; normality tested with d'Agostino & Pearson  
1317 test. n=4 patients in each histopathology group (ALV, DAD and OP).
- 1318 D. C-reactive protein (CRP) levels closest to the point of sampling and corresponding  
1319 histopathology state in lung sections. Median and IQR shown, p value calculated using Kruskal-  
1320 Wallis test with Dunn's multiple comparison test. n=4 patients in each histopathology group  
1321 (ALV, DAD and OP). Source data are provided in the Source Data File.

1322

1323 **Fig. 2. High definition immunophenotyping of lung cells and identification of tissue structure**

1324

- 1325 A. UMAP representation of myeloid, lymphocyte and structural cell 'mega clusters' from all  
1326 regions of interest (ROI) (k = 30) (COVID-19 and HC). See also Supplementary Fig. 7 for extended  
1327 analysis steps. HC – healthy control.
- 1328 B-C. Number of cells per mm<sup>2</sup> of lung tissue sections in all COVID-19 samples (n=12 patients, 30  
1329 ROIs' in total) compared to healthy control (HC) samples (n=2 individuals, 4 ROIs in total).  
1330 Median shown, error bars are IQR. n=524,552 cells in total for COVID-19 samples, n= 30,053

1331 cells for HC. Statistical analysis performed after samples grouped into histopathology states  
1332 (see Fig. 3D). Source data are provided in the Source Data File.

1333

1334 D-E. Immunofluorescence (IF) staining validation for Neut\_CD8\_ADJ cell cluster and  
1335 Mono\_CD31\_ADJ cell clusters. Small panels are high magnification confocal images showing  
1336 CD8 and CD15 staining (top small panel), and CD14 and CD31 staining (bottom small panel) on  
1337 adjacent cells. Broken yellow circles show CD8 T cell (white- CD8) – neutrophil (green-CD15)  
1338 couplets throughout lungs (D); and CD14-staining cells next to CD31-expressing cells  
1339 (endothelium) in lung tissue (E). See also Supplementary Fig. 6 for negative controls. IF images  
1340 shown are representative of lung sections from n=3 patients; staining experiment performed  
1341 once per lung sections.

1342 F. Heatmap of median scaled intensity for each marker for all cell clusters in the ‘Myeloid’ mega  
1343 cluster. ‘n\_cells’ - average number of cells in all COVID-19 ROIs. Total cells – 171, 777. UD –  
1344 undefined cluster

1345 G-H. Exemplar MCD image from 37-plex imaging mass cytometry (IMC) staining of a DAD ROI  
1346 showing expression of CD8 T cells (CD8 -green), neutrophils (CD15-red) and CD8\_CD15\_ADJ  
1347 cell clusters (green and red co- expression, making yellow). Image is one of n=26 ROIs, some  
1348 of which do not have the CD8\_CD15\_ADJ cell clusters – see Fig. 3B for number of ROIs showing  
1349 presence of this cell cluster in all ROIs (n=26 COVID-19; n=4 HC). H - Same MCD images as (G)  
1350 but with IFN- $\beta$  channel ‘open’ (white) showing IFN- $\beta$  expression on Neut\_CD8\_ADJ (yellow).

1351 I. Higher magnification of a set of 3 MCD panels - ‘none’ - Neut\_CD8\_ADJ (yellow) only (arrows);  
1352 ‘IFN- $\gamma$ ’ – with ‘IFN- $\gamma$ ’ (white) channel opened on MCD viewer showing expression on  
1353 Neut\_CD8\_ADJ (yellow) (arrows) and some CD8 (green); ‘GZB’ - with ‘GZB’ (cyan) channel  
1354 opened and showing expression on Neut\_CD8\_ADJ (yellow) (arrows). CD172a panel shows  
1355 confocal immunofluorescence staining (white) on CD15 and CD8 adjacent to each other. IF  
1356 images shown are representative of lung sections from n=3 patients; staining experiment  
1357 performed once per lung sections. ALV – alveolitis, DAD – diffuse alveolar damage, OP -  
1358 organising pneumonia. MCD images from all 26 ROIs (n=10 ALV, n=8 DAD and n=8 OP) were  
1359 analysed and median expression intensity for all ROIs shown in (F) and Supplementary Fig. S7.  
1360 All scale bars in  $\mu\text{m}$ .

1361

1362 **Fig. 3. Quantification of immune and structural cells in COVID-19 lungs**

1363 A-C. Cell abundance plots for immune cells (myeloid and lymphoid cells) and structural cells in lung  
1364 tissue, adjusted for surface area in COVID lungs categorised into those with histopathology



1365 states of alveolitis(ALV) (n=4 patients, 10 ROIs), diffuse alveolar damage (DAD) (n=4 patients,  
1366 8 ROIs) and organising pneumonia (OP) (n=4 patients, 8 ROIs), compared to healthy control  
1367 (n=2 individuals, 4 ROIs). Line in figure represents median. See Supplementary Table 4 for  
1368 extended phenotypic description for all cell types and clusters. Source data are provided in the  
1369 Source Data File.

1370

1371 D. Heatmap of fold change (FC) difference in abundance of cell types for COVID-19 samples (ALV,  
1372 DAD and OP) vs healthy controls (HC) depicted in (A). Asterisks show those with significant  
1373 differences - adjusted p-values are \* $p < 0.05$  \*\* $p < 0.01$  \*\*\* $p < 0.001$ , calculated using code from  
1374 the diffcyt R package (version 1.8.8) with the option testDA\_edgeR; two-sided analysis  
1375 employed, and multiple comparisons adjusted using Benjamini-Hochberg method . Arrow  
1376 refers to immune cells that showed progressive increase in abundance with progression  
1377 histopathology states from ALV to OP.

1378

1379 **Fig. 4. Spatial analysis of immune and structural cells in COVID-19 lungs**

1380 A. Schematic representation of the sequential spatial analysis of cellular co-location, starting  
1381 with quadrat correlation matrix (QCM), then cross pair correlation function (cross-PCF)  
1382 analysis, interrogation of cross-PCF output and organization according to main questions.  
1383 QCM output is provided in Supplementary Fig. 8.

1384 B.  $g(r=20)$  heatmaps showing statistically significant correlated pairs of cells derived from QCM  
1385 and cross-PCF analysis (see Methods for full description).  $n=479,349$  single cells from  $n=12$   
1386 COVID patients' lung sections ( $n=26$  ROIs); in total,  $n=144,937$  cells in ALV,  $n=146333$  in DAD  
1387 and  $n=163,506$  in OP. Red boxes indicate groups of cell subsets from the same immune  
1388 phenotype – neutrophils (Group 1), monocytes and macrophages (Group 2), CD3 T cells  
1389 (Group 3) and MAIT cells (Group 4).

1390

1391 **Fig. 5. Spatial organization of immune cells around structural cells in COVID-19 lungs**

1392 A-B. Spatial connectivity plots for proliferating alveolar epithelium, showing immune cells that are  
1393 significantly co-located to proliferating alveolar epithelium (designated 'anchor cell') in the three  
1394 histopathology states. The size of the nodes (filled-in circle) represents mean cell counts  
1395 (abundance) for the specified cell cluster for all the ROIs in the histopathology state (scale shown  
1396 in grey), and colour of nodes relate to histopathology state. Connecting lines indicate a  
1397 statistically significant co-location between the two cell types derived from QCM and cross-PCF  
1398 analyses. The thickness of the lines relates to the  $g(r=20)$  value relative to each pair in the plot –

1399 the thicker the line, the higher the  $g(r=20)$  and therefore greater strength of co-location between  
1400 the immune cell type and anchor cell.  $n=479,349$  single cells from  $n=12$  COVID patients' lung  
1401 sections ( $n=10$  ROIs for ALV;  $n= 8$  DAD;  $n= 8$  OP);  $n=144,937$  cells in ALV,  $n=146333$  in DAD and  
1402  $n=163,506$  in OP.

1403 C-D. Histogram shows % of two anchor cells – proliferating alveolar epithelial (PAE) cells (C) and  
1404 endothelial cells (D) that are in contact with specified immune cell type. Source data are provided  
1405 in the Source Data File.

1406 E-F. Cross-PCF profiles for the two most abundant co-located structure:immune cell pairs in DAD.  
1407 Curves show the change in  $g(r)$  along the radius( $r$ ) from anchor cells [proliferating alveolar  
1408 epithelium (prolif alv epit) and endothelial cells (endo)] for Neut-CD8\_ADJ cell clusters and  
1409 Mono\_CD31\_ADJ cell clusters respectively. Blue coloured area around curve is the 95%  
1410 confidence interval for  $n=8$  ROIs with DAD.

1411 G. Radial connectivity map depicting all statistically significant pairs of structure:immune cells in all  
1412 histopathology states; anchor cells (structural cells) are in smaller, inner circle.  $n=479,349$  single  
1413 cells from  $n=12$  COVID patients' lung sections ( $n=10$  ROIs for ALV;  $n= 8$  DAD;  $n= 8$  OP). 'DR<sup>hi</sup> BE'  
1414 – HLADR<sup>hi</sup> bronchial epithelium; 'DR<sup>lo</sup> BE' – HLA DR<sup>lo</sup> bronchial epithelium; "Endo'- endothelial  
1415 cells; 'PAE'- 'proliferating alveolar epithelium', 'PBE' – 'proliferating bronchial epithelium'; 'PE' –  
1416 'proliferating endothelium' 'BV' – 'blood vessels'. Numerical values indicate  $g(r=20)$  for that pair  
1417 in that state (coloured bar), and % indicates proportion of anchor cells that are co-located with  
1418 the specified immune cells.

1419 H. Topographical correlation map showing distribution of the co-located Neut\_CD8\_ADJ cluster and  
1420 proliferating alveolar epithelial cell pair (left panel) in an exemplar tissue (an ROI with DAD). Cells  
1421 of type A (e.g. Neut\_CD8\_ADJ) are positively ( $\Gamma_{ab} \gg 0$ ) or negatively ( $\Gamma_{ab} \ll 0$ ) associated with  
1422 cells of type B (e.g. Proliferating alveolar epithelium) (see Methods)

1423 I. MCD images showing Neut\_CD8\_ADJ clusters amidst single CD8<sup>+</sup> T cells, CD15<sup>+</sup> immature  
1424 neutrophils and epithelial markers (EpCAM and PanCK). Couplets of CD8<sup>+</sup> and CD15<sup>+</sup> cells -  
1425 Neut\_CD8\_ADJ clusters (red and green merging to form yellow cells) (arrows) are most clearly  
1426 visible in DAD. Exemplar section is shown from analyses of  $n=10$  ALV ROIs,  $n=8$  DAD ROIs and  
1427  $n=8$  OP ROIs ( $n=12$  patients). Sections were stained once with 37 plex panel.

1428

#### 1429 **Fig. 6. Spatial organization amongst immune cells in COVID-19 lungs**

1430 A-C. Radial connectivity map depicting all statistically significantly co-located pairs of immune-  
1431 immature neutrophil subsets (including ADJ subsets) (A) immune-monocyte subsets (B and C,  
1432 separated for clarity) cells in all histopathology states ( $n=10$  ALV,  $n=8$  DAD and  $n=8$  OP). Anchor

1433 cells (immature neutrophil and monocyte subsets) are in smaller, inner circle. Numerical values  
1434 indicate  $g(r=20)$  for that pair in that state (coloured bar), and % indicates proportion of anchor  
1435 cells that are co-located with the specified immune cells. These significantly co-located pairs of  
1436 cells are derived from  $n=479,349$  single cells in all ROIs from  $n=12$  COVID patients' lung sections  
1437 ( $n=10$  ROIs for ALV;  $n= 8$  DAD;  $n= 8$  OP);  $n=144,937$  cells in ALV,  $n=146333$  in DAD and  $n=163,506$   
1438 in OP (see Methods for 3-step mathematical algorithm for determining statistical significance of  
1439 co-location).

1440

1441 D-E. Spatial connectivity plots for Neut\_CD8\_ADJ (D) and Mono\_CD31\_ADJ (E), showing immune  
1442 cells that are statistically significant co-located to proliferating alveolar epithelium (designated  
1443 'anchor cell') in the three histopathology states (see Methods for 3-step mathematical algorithm  
1444 for determining statistical significance of co-location). Size of nodes (filled-in circle) represent  
1445 mean cell counts for the specified cell cluster for all the ROIs in the histopathology state, and  
1446 colour of nodes relate to histopathology state. Connecting lines indicate a statistically significant  
1447 co-location between the two cell types derived from QCM and cross-PCF analyses. Thickness of  
1448 line relate to value of  $g(r=20)$  relative to each pair in the plot – the thicker the line, the higher the  
1449  $g(r=20)$  and strength of co-location between the immune cell type and anchor cell.

1450 F. Adjacency cell network (ACN) map showing contact between the Mono\_CD31\_ADJ cluster,  
1451 Neut\_CD8\_ADJ cluster and proliferating alveolar epithelial. Cell segmentation masks generated  
1452 by DeepCell were used to produce this spatially-embedded network in which nodes represent  
1453 centres of cell types (e.g. green – Neut\_CD8\_ADJ cell cluster). Nodes are connected by a line if  
1454 the corresponding cells in the segmentation mask share a border.

1455 G. MCD image showing CD8 (green), CD15(red) and CD15 and CD8 co-staining (yellow) (representing  
1456 Neut\_CD8\_ADJ cell clusters) amidst endothelial cells (CD31 staining in turquoise) and monocytes  
1457 (CD14 staining in purple) in a lung section with DAD on histopathology analysis. Exemplar ROI is  
1458 shown for (F) and (G), out of 26 ROIs stained, from 12 patients ( $n=10$  ALV ROI,  $n=8$  DAD and  $n=8$   
1459 OP).

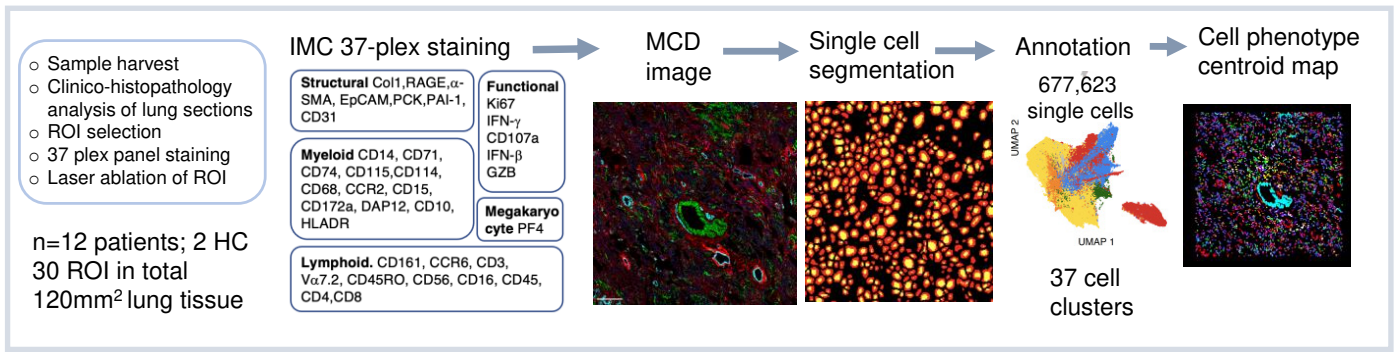
1460

1461 **Fig. 7**

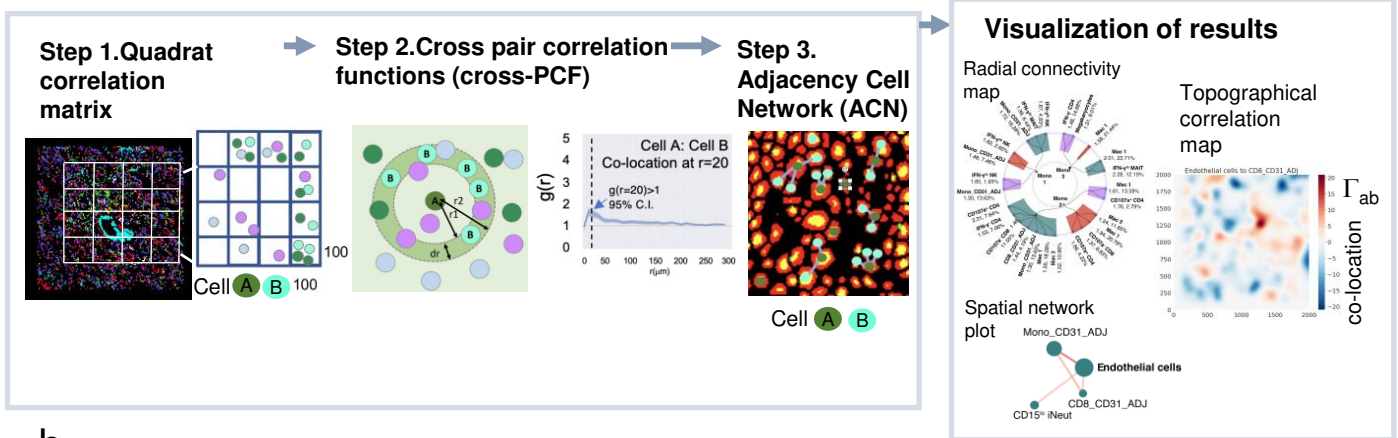
1462 A. SCMAP matching heatmaps representing the Jaccard indices of similarity between COMBAT  
1463 (blood)<sup>6</sup> and COSMIC (lung) lymphocyte clusters.  $CD107a^-$  CD8 T cell and  $CD107a^+$  CD8 T cell in  
1464 COSMIC matched to blood GZB<sup>+</sup> CD8 T cells in COMBAT.  $IFN-\gamma^+$  CD4 T cells matched to COMBAT's  
1465 'activated CD4 T cells'

1466 B. SCMAP matching heatmaps representing the Jaccard indices of similarity between COMBAT  
1467 (blood) and COSMIC (lung) myeloid clusters. Mono\_CD31\_ADJ and Mono\_PAI-1\_ADJ and all  
1468 macrophage subsets matched with HLA DR<sup>hi</sup> classical monocytes in the blood from COMBAT data  
1469 C. UMAP representation of neutrophils from controls and COVID-19 infected patients (n=2,776,928  
1470 single cells from n=77 COVID-19 patients and 11 healthy volunteers (HV), down sampled to 100  
1471 000 cells per condition) obtained from COMBAT consortium, showing 8 subsets of neutrophils.  
1472 D. Heatmap showing median marker expression for genes (selected to match COSMIC's key protein  
1473 expression on neutrophils) on the 8 neutrophil subsets, demonstrating high similarity of marker  
1474 expression in immature neutrophil 2 (iNeut2) in COMBAT (blood) with Neut\_CD8\_ADJ in COSMIC  
1475 (lung) (See also Fig. 2F).  
1476 E. Abundance of the 8 neutrophil subsets in blood as % of total neutrophils, from healthy volunteers  
1477 (HV), mild, severe and critical COVID-19 patients from the COMBAT consortium showing a  
1478 progressive increase in immature 2 neutrophils with increasing COVID-19 disease severity. HV  
1479 (n=11), mild (n=18), severe (n=41), critical (n=18) patients, n=1 experiment. The boxplot is  
1480 median, with IQR; whiskers are the range or 1.5\*IQR (whichever is smaller). Composition  
1481 analysis was performed using scCODA with inbuilt adjustment for multiple comparison<sup>70</sup>.  
1482 Credible compositional changes were identified comparing all groups to HV and FDR<0.1  
1483 is marked with #. Source data are provided in Source Data File.  
1484  
1485  
1486  
1487

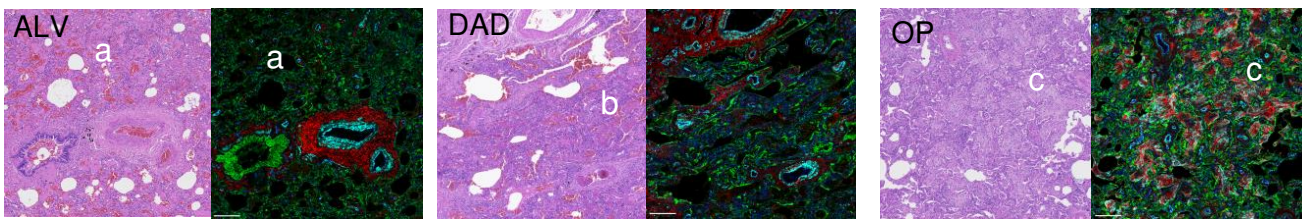
a.



**Statistical quantification of spatial co-location of cells**



b.



$\alpha$ -SMA Epcam/PanCK Collagen CD31 Scale Bar 200 $\mu$ m

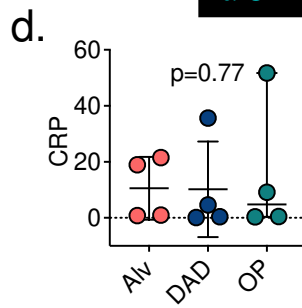
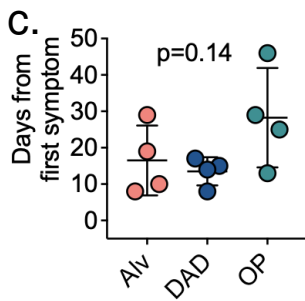


Figure 1

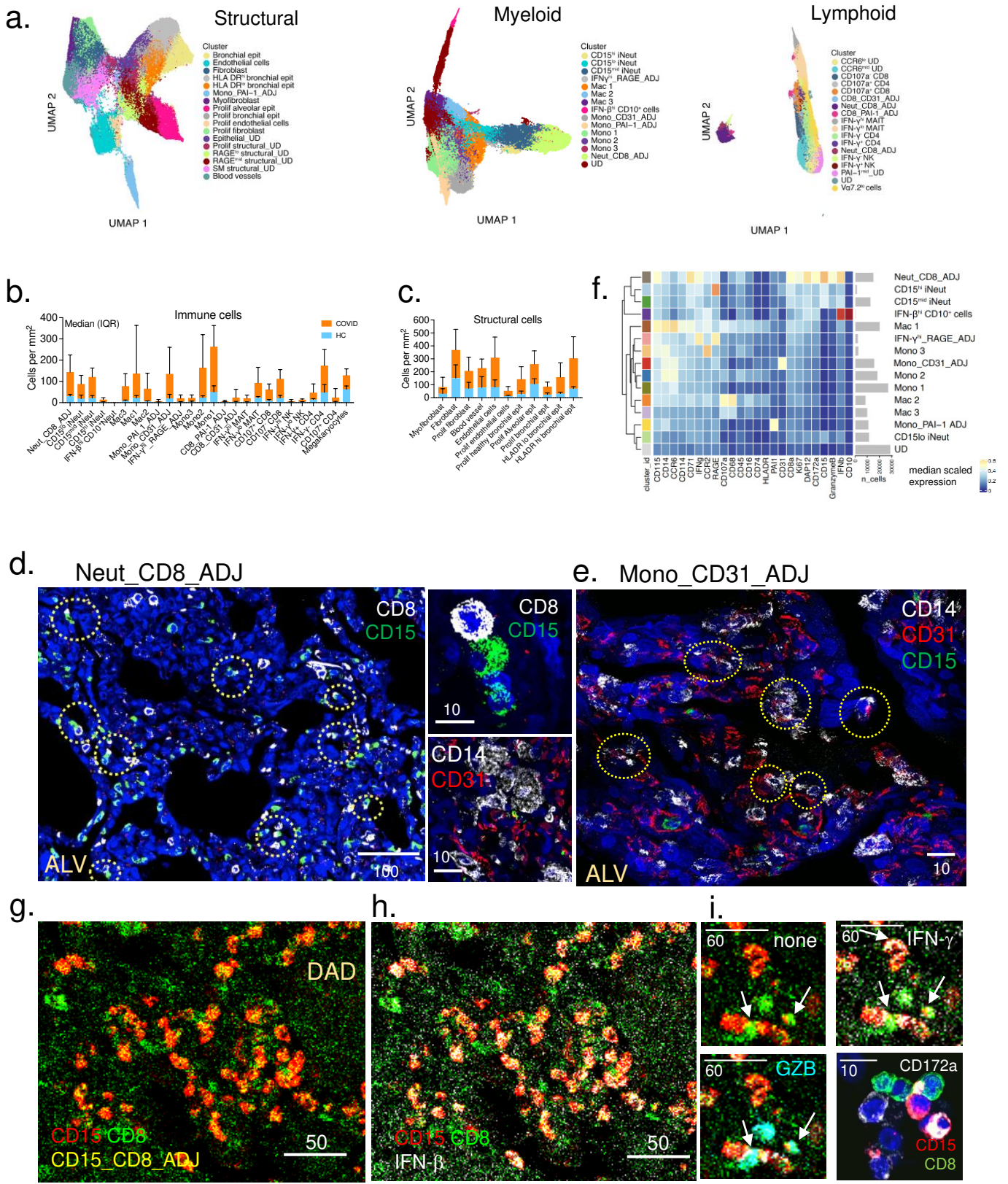


Figure 2

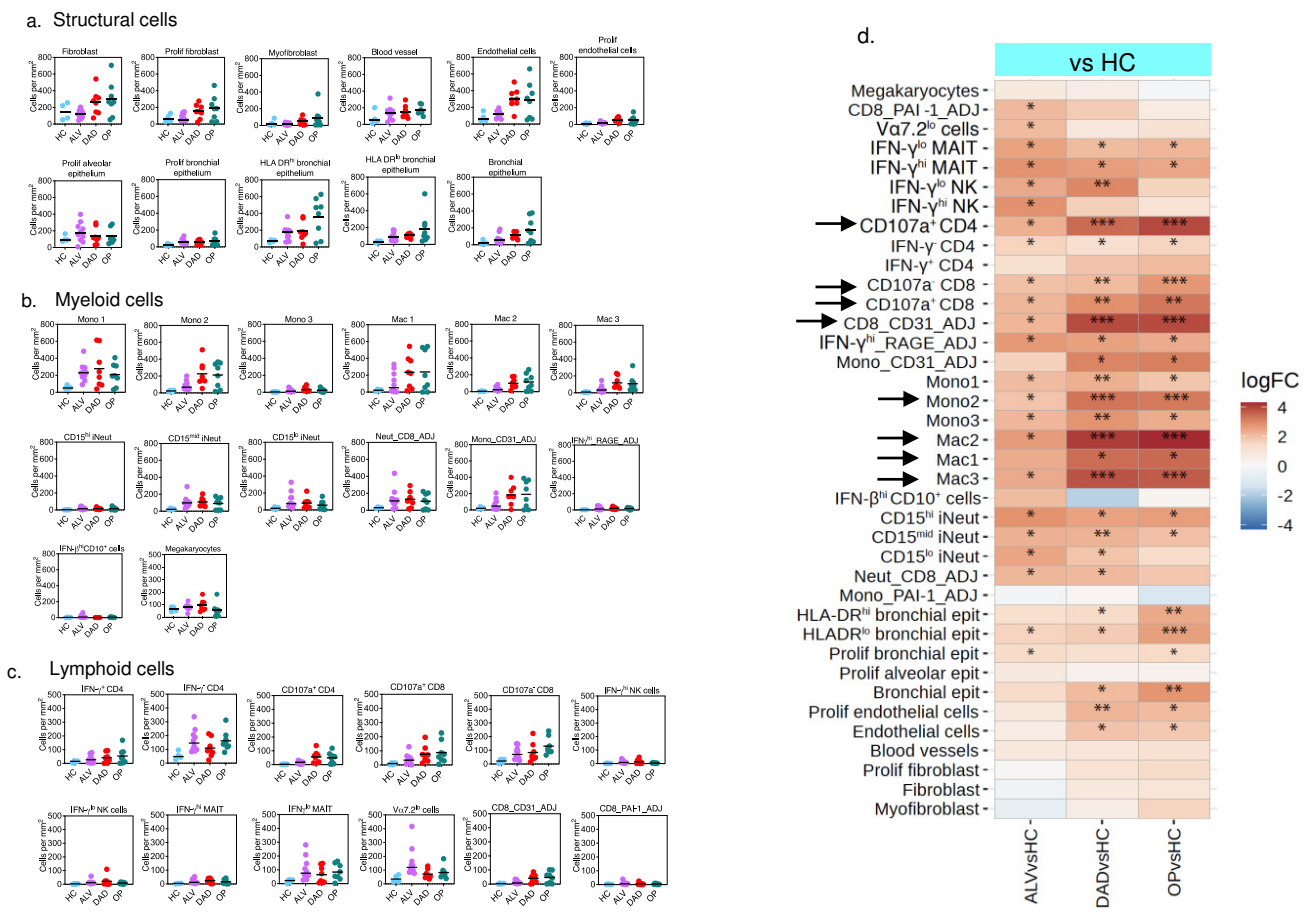


Figure 3

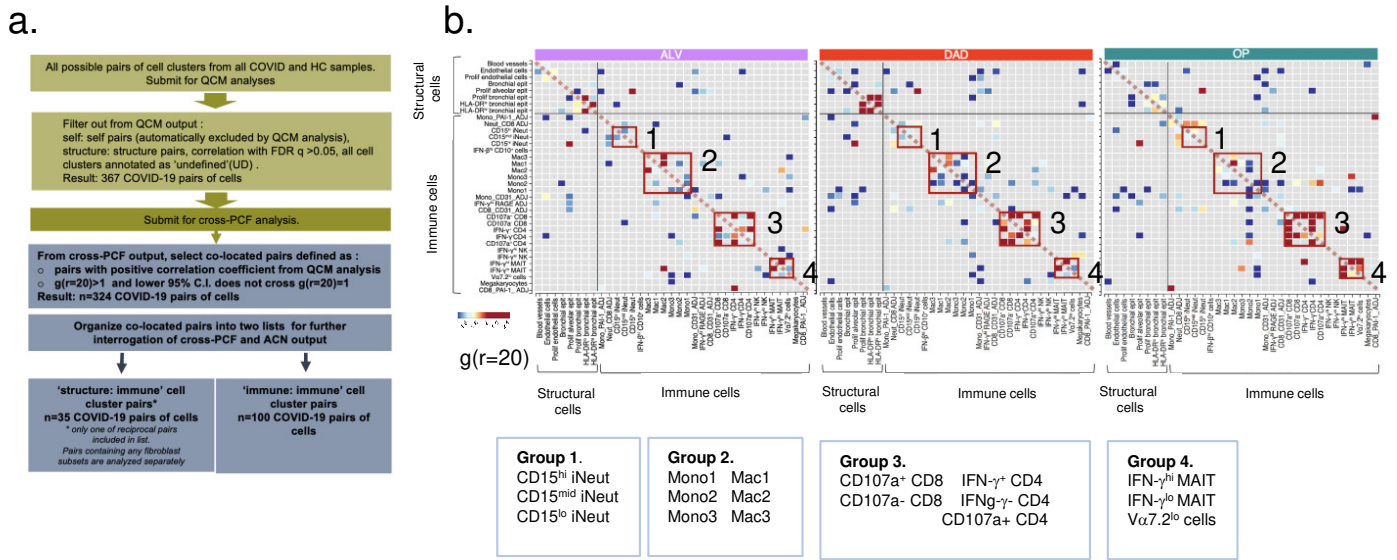
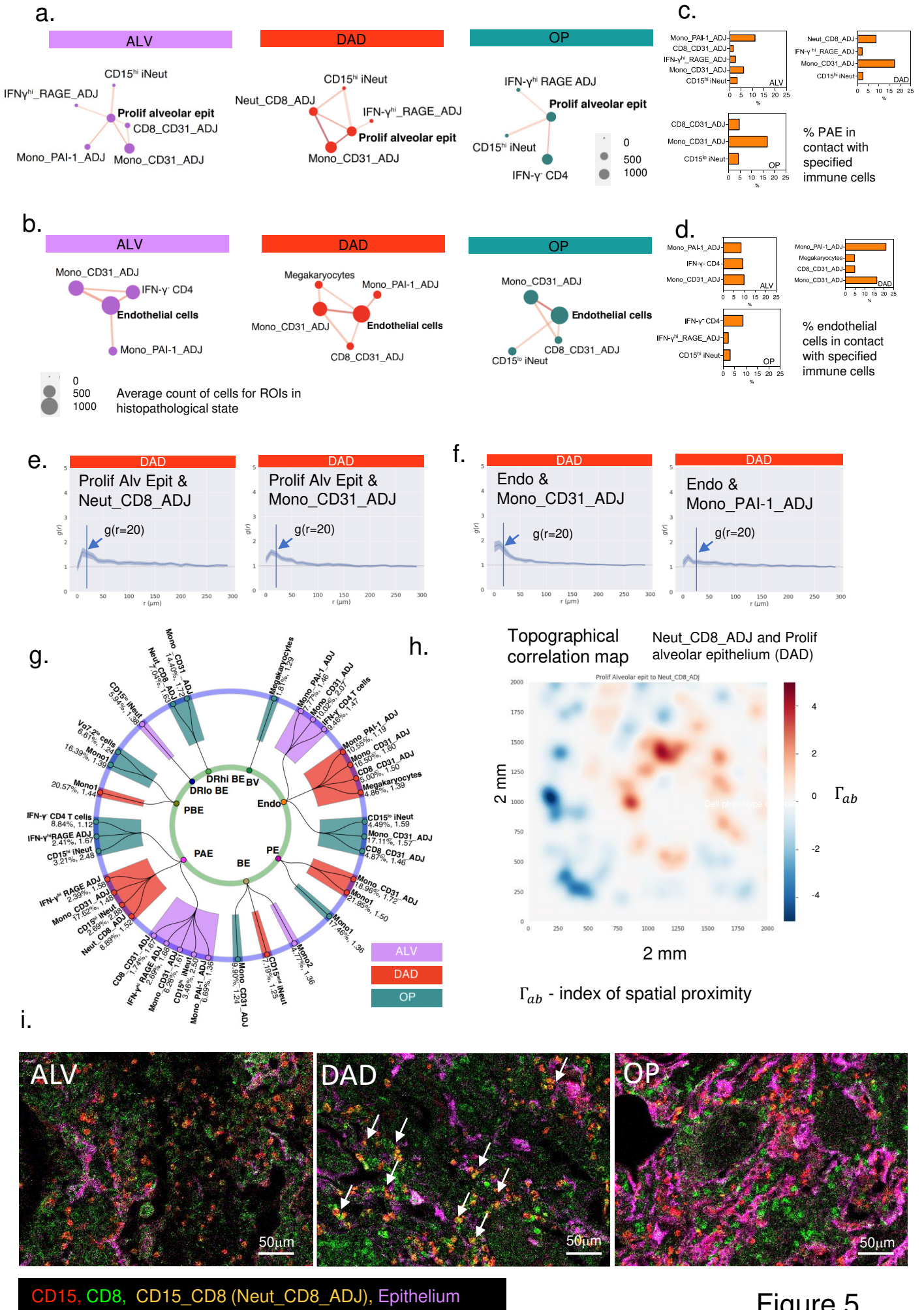
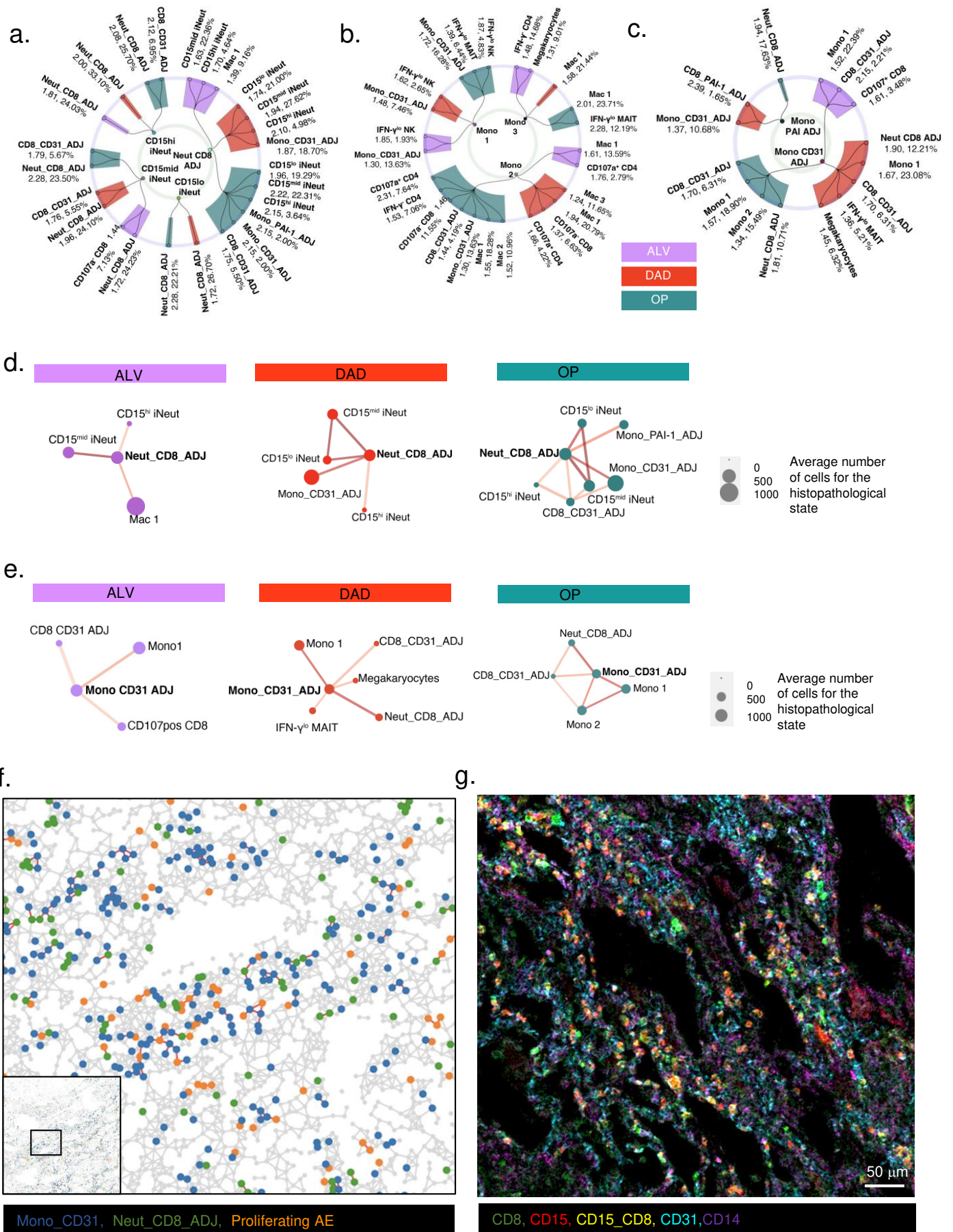


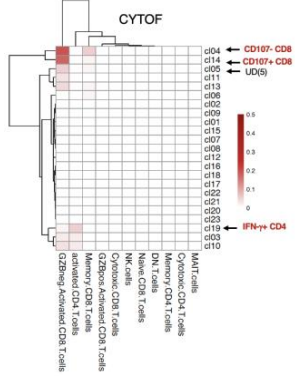
Figure 4



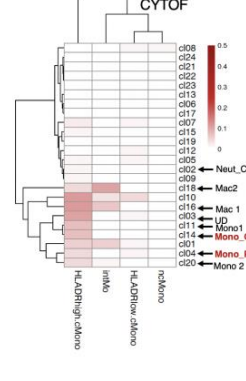




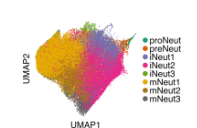
**a. Lymphoid mapping**



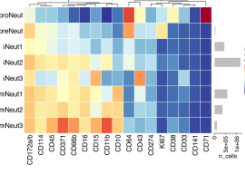
**b. Myeloid mapping**



**c.**



**d.**



**e.**

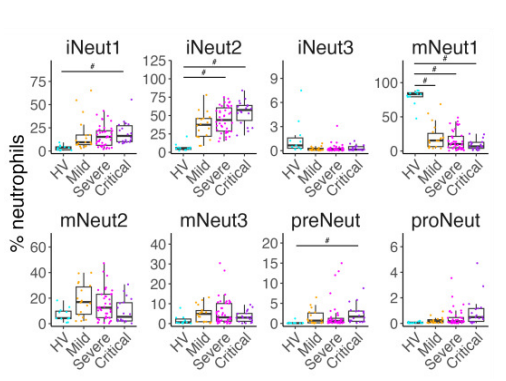


Figure 7

| Name of software                  | Source  | Identifier  |
|-----------------------------------|---|---|
| imctools                          | <a href="https://github.com/BodenmillerGroup/imctools">https://github.com/BodenmillerGroup/imctools</a>   | RRID:SCR_017132   |
| Deepcell                          | <a href="https://vanvalen.github.io/about/">https://vanvalen.github.io/about/</a>   | RRID:SCR_022197   |
| Phenograph                        | <a href="https://github.com/JinmiaoChenLab/Rphenograph">https://github.com/JinmiaoChenLab/Rphenograph</a>   | RRID:SCR_016919   |
| Harmony                           | <a href="https://github.com/slowkow/harmony">https://github.com/slowkow/harmony</a>   | RRID:SCR_022206   |
| Slingshot                         | <a href="https://github.com/kstreet13/slingshot">https://github.com/kstreet13/slingshot</a>   | RRID:SCR_017012   |
| Ruffus                            | <a href="http://www.ruffus.org.uk/">http://www.ruffus.org.uk/</a>   | RRID:SCR_022196   |
| QuPath                            | <a href="https://qupath.github.io/">https://qupath.github.io/</a>   | <a href="https://doi.org/10.1038/s41598-017-17204-5">https://doi.org/10.1038/s41598-017-17204-5</a> |
| MCD                               | <a href="https://www.standardbio.com/products-services/software">https://www.standardbio.com/products-services/software</a>                             | RRID:SCR_023007   |
| Catalyst R                        | <a href="http://bioconductor.org/packages/CATALYST/">http://bioconductor.org/packages/CATALYST/</a>   | RRID:SCR_017127   |
| Harmony                           | <a href="https://github.com/immunogenomics/harmony">https://github.com/immunogenomics/harmony</a>   | RRID:SCR_022206   |
| diffcyt R package (version 1.8.8) | <a href="https://www.bioconductor.org/packages/release/bioc/html/diffcyt.html">https://www.bioconductor.org/packages/release/bioc/html/diffcyt.html</a> | RRID:SCR_023006   |

**Table 1** Software and algorithms used in data analysis.